

# Axisymmetric semi-analytical finite elements for modelling waves in buried/submerged fluid-filled waveguides

Michał K. Kalkowski\*, Jennifer M. Muggleton, Emiliano Rustighi

*Institute of Sound and Vibration Research, University of Southampton, Highfield, Southampton SO17 1BJ, UK*

---

## Abstract

Efficient and accurate predictions of wave propagation are a vital component of wave-based non-destructive interrogation techniques. Although a variety of models are available in the literature, most of them are suited to a particular wave type or a specific frequency regime. In this paper we present a multi-wave model for wave propagation in axisymmetric fluid-filled waveguides, either buried or submerged in a fluid, based on the semi-analytical finite elements. The cross-section is discretised with high-order spectral elements to achieve high efficiency, and the singularities resulting from adopting a Lobatto scheme at the axis of symmetry are handled appropriately. The surrounding medium is modelled with a perfectly matched layer, and a practical rule of choice of its parameters, based only on the material properties and the geometry of the waveguide, is derived. To represent the fluid and the solid-fluid coupling, an acoustic SAFE element and appropriate coupling relationships are formulated. The model is validated against both numerical results from the literature and experiments and the comparisons show very good agreement. Finally, an implementation of the method in Python is made available with this publication.

*Keywords:* wave propagation, waves in pipes, fluid-filled pipes, waves in embedded pipes, semi-analytical finite element, perfectly matched layer, spectral elements

---

## 1. Introduction

Acoustic waves are perhaps the most common principle upon which modern non-destructive interrogation methods for buried/immersed pipes are developed [1, 2]. Both wavespeed and attenuation depend on the properties of the pipe, its contents, and the surrounding medium, and can be used to identify these properties or evaluate their change over time. Moreover, when incident upon a discontinuity, either in the pipe or in the surrounding medium, the waves scatter, allowing for detection of

---

\*Corresponding author, currently at the Department of Mechanical Engineering, Imperial College, London SW7 2AZ, UK  
*Email address:* M.Kalkowski@imperial.ac.uk (Michał K. Kalkowski)

<sup>1</sup>This is an accepted manuscript with minor corrections published in *Computers and Structures* (2017), <https://doi.org/10.1016/j.compstruc.2017.10.004>.

<sup>2</sup>This manuscript version is made available by the author under the CC-BY-NC-ND 4.0 license <http://creativecommons.org/licenses/by-nc-nd/4.0/>

defects or a weakened support. Finally, waves radiating from the pipe can be sensed at a ground surface and provide a basis upon which both the location and the condition of the pipe can be assessed. An essential ingredient for all these techniques is a reliable model for wave propagation in buried/submerged pipes with fluid. Although there is a considerable number of publications dealing with either waves in fluid-filled pipes or with waves in embedded cylinders, relatively few works tackle the complete problem that includes both the pipe, the fluid and the surrounding medium.

For obvious historical reasons, analytical approaches were developed first. Dispersion curves and energy distributions for fluid-filled thin cylinders have been presented by Fuller and Fahy [3]. Pinnington and Briscoe derived low frequency approximations for both fluid-dominated and axial waves in free pipes. The effect of the surrounding fluid was investigated by e.g. Greenspon [4] and Sihna et al. [5]. The case of a solid medium restraining the pipe has been studied to some extent by Toki and Hakada [6] (in an earthquake engineering context) and by Jette and Parker [7].

The pipe, the surrounding medium and the contained fluid altogether were considered probably for the first time by Muggleton et al. [8–10] where both fluid-dominated and axial waves were studied based on a simplified interaction between the pipe and the soil/water. Subsequent refinements and extensions of that model allowing for inclusion of the shear coupling with lubricated contact [11], compact contact [12] and evaluating torsional waves [13] have also been published.

Despite the negligible computational cost and an immediate insight into the physics gained from closed-form expressions offered by the aforementioned models, they are often limited to a particular wave type and the low frequency range. A more versatile approach based on the global matrix method [14] was developed in the ultrasonic community and was successfully applied to the problem of embedded, fluid-filled cylinders [15, 16], among others. The global matrix method originates from the description of the motion of the structure as a superposition of bulk waves propagating in each layer (the number of layers and materials can be arbitrary). The fundamental formulation is analytical, but requires a numerical solution in the form of root-tracing which often offers a fast and accurate solution. However, for complex structures, root-tracing may become both inefficient and unreliable (as it strongly depends on the initial guess). Moreover, developing a universal tracing algorithm applicable to all configurations is a rather cumbersome task.

The limitations of analytical models can be circumvented with numerical methods which solve the dispersion equation as an eigenvalue problem, such as the semi-analytical finite element (SAFE) method. The fundamental concept behind SAFE is that the cross-section is discretised using finite elements and spatially harmonic motion is assumed in the direction of propagation [17, 18]. The governing equation is written as an eigenvalue problem which can easily be solved using any numerical package available. SAFE provides a stable and reliable solution at a cost of the finite element discretisation. However, the number of degrees of freedom is usually small for closed waveguides.

Modelling open (embedded) waveguides with SAFE raises several new challenges, of which the greatest is an efficient representation of the surrounding medium. Castaigns and Lowe [19] proposed the idea of an absorbing layer with material damping smoothly increasing away from the core. Their

approach could be conveniently implemented in a commercial finite element package, but the size of the problem grew large for low wavespeed soils. Jia et al. [20] developed infinite elements that can be coupled to standard, solid SAFE elements and analysed the effect of soil on waves in hollow cylinders. Mazzotti et al. developed a hybrid approach based on SAFE and 2.5D boundary element method [21–23]. This idea yielded very promising results and was validated with experiments. However, coupling of two quite complex methods poses additional challenges for implementation.

An alternative is to use perfectly matched layers (PML) to represent the embedding medium. PMLs were first used in mid 1990s [24] and have since been successfully applied to a number of applications, particularly in the electromagnetic community. Including PMLs in numerical models for elastic waves is a relatively new idea. Treyssède et al. [25] developed a SAFE-PML formulation for plate like structures with a cubic polynomial chosen as a stretching function. Soon after, Nguyen et al. [26] presented an analogous formulation applied to three-dimensional embedded waveguides. However, for an acoustically slow surrounding medium, the size of the problem could grow large owing to short bulk wavelengths. As a remedy, Treyssède [27] applied spectral elements utilising high-order polynomials to enhance the efficiency of the solution. Also recently, Duan et al. [28] developed an axisymmetric SAFE-PML formulation and proposed the use of an exponential stretching function, particularly well suited to wave problems.

To enable SAFE-PML calculations to be configured rapidly, Zuo et al. [29] implemented this model in a commercially available software. The advantages of their approach are that one can benefit from the readily available meshing tools and can conduct simulations without writing any code. The authors also give guidelines on the choice of PML parameters. Some numerical examples for solid 1D and 2D cross-sections have also been presented. Despite, its user-friendliness, this approach still yields problems of considerable size.

A scaled boundary finite element method (SBFEM) is a good alternative to SAFE and has recently been applied to the problem of axisymmetric [30] and embedded waveguides [31–33]. SBFEM is a well-established numerical framework, particularly in earthquake engineering. Its key concept is to represent the computational domain using a discretised boundary and a scaling centre. For guided wave problems, the final form of the equations bears many similarities with those coming from SAFE, since in both cases the assumption of the harmonic variation of the displacement along the propagation direction is adopted. However, the key concept and the origin of SBFEM are inherently different from FEM. In the references mentioned above, the authors simplified the problem by representing the surrounding medium with a dashpot boundary condition. Although their approach is simple and elegant, it cannot provide accurate results when the contrast between acoustic impedances is low.

Despite the impressive developments in the field of modelling of elastic waves in recent decades, to the best of authors' knowledge, no complete and efficient numerical model for waves in fluid-filled embedded/submerged pipes has been published <sup>3</sup>. This paper proposes a SAFE formulation capable

---

<sup>3</sup>We acknowledge, that during the review process of this manuscript, Zuo and Fan [34] published an article on SAFE-PML

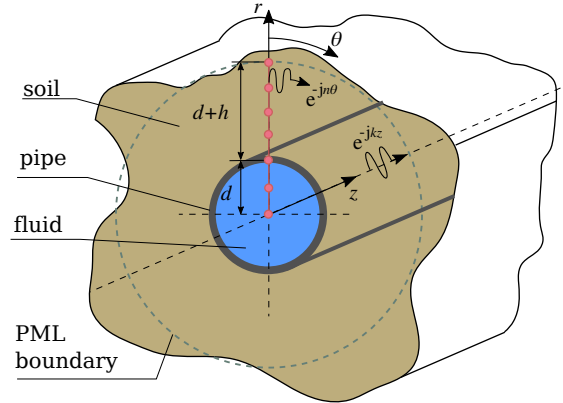


Figure 1: Schematic diagram outlining the problem and chosen coordinate conventions.

of representing the structural-acoustic coupling and benefiting from the circumferential periodicity assumption. Both the pipe and the surrounding medium can be composed of a number of layers of different, generally anisotropic materials. We use high-order spectral elements (SEs), as they are better suited to wave propagation problems than standard finite elements and allow for efficient simulations. The singularities arising from the axisymmetric assumption applied to SEs are accounted for appropriately. The surrounding medium, which can be either solid or fluid, is represented by a perfectly matched layer and practical guidelines for the choice of the parameters of the PML are derived. Our formulation is validated against published numerical results and experimental measurements showing very good agreement. Finally, an implementation of the proposed method in Python is made available with this publication.

## 2. Derivation of SAFE elements

We consider an axisymmetric, infinitely long and uniform waveguide, where  $r$  and  $\theta$  are the cross-sectional coordinates and  $z$  is the direction of propagation. The waveguide can be composed of any number of layers, either solid or fluid. Owing to the axisymmetric assumption the cross-section is represented with mono-dimensional elements. A practical representation of such class of problems is an embedded/submerged fluid-filled pipe. The pipe scenario together with chosen labelling and conventions is shown in Fig. 1. SAFE formulations for all respective elements are presented in the following subsections.

### 2.1. Structural element

The structural (elastic) SAFE element is derived in a similar way to [18] but with slightly different conventions. We start from recalling the virtual work principle for deformable elastic bodies [35] which

---

modelling of structures immersed in a fluid, which bears some similarities with the approach presented in this paper.

states that

$$\int_V \delta \bar{\mathbf{u}}^\top \rho \ddot{\bar{\mathbf{u}}} dV + \int_V \delta \bar{\boldsymbol{\epsilon}}^\top \bar{\boldsymbol{\sigma}} dV = \int_V \delta \bar{\mathbf{u}}^\top \bar{\mathbf{t}} dV \quad (1)$$

where  $V$  is the volume occupied by the waveguide,  $\bar{\mathbf{u}}$  is the displacement vector,  $\rho$  is the mass density,  $\bar{\boldsymbol{\epsilon}}$  is the strain vector,  $\bar{\boldsymbol{\sigma}}$  is the stress matrix,  $\bar{\mathbf{t}}$  is the external traction and  $(\ddot{\cdot})$  symbol denotes double differentiation with respect to time. Our attention is focused on free wave propagation here, hence the right-hand side, i.e. the external traction, is set to zero.

The displacement and strain vectors are defined as

$$\begin{aligned} \bar{\mathbf{u}} &= [\bar{u}_r \quad \bar{u}_\theta \quad \bar{u}_z]^\top \\ \bar{\boldsymbol{\epsilon}} &= [\bar{\epsilon}_{rr} \quad \bar{\epsilon}_{\theta\theta} \quad \bar{\epsilon}_{zz} \quad \bar{\gamma}_{\theta z} \quad \bar{\gamma}_{zr} \quad \bar{\gamma}_{r\theta}]^\top \end{aligned} \quad (2)$$

where  $\gamma$  are the engineering shear strains. The stress is related to the strain via the Hooke's Law:

$$\bar{\boldsymbol{\sigma}} = \mathbf{C} \bar{\boldsymbol{\epsilon}} \quad (3)$$

with  $\mathbf{C}$  being the elasticity matrix.

For the considered axisymmetric geometry, the displacement is assumed to be circumferentially periodic, which is expressed using a Fourier series

$$\bar{\mathbf{u}}(r, \theta, z) = \sum_{n=0}^{\infty} \bar{\mathbf{u}}_n(u, z) e^{-jn\theta} \quad (4)$$

where  $n$  is an integer to ensure  $2\pi$ -periodicity. For clarity, this assumption is not applied till the end of the derivation.

The strain is related to the displacement via differential operators:

$$\bar{\boldsymbol{\epsilon}} = \left( \frac{1}{r} \mathbf{L} + \mathbf{L}_r \frac{\partial}{\partial r} + \mathbf{L}_\theta \frac{1}{r} \frac{\partial}{\partial \theta} + \mathbf{L}_z \frac{\partial}{\partial z} \right) \bar{\mathbf{u}} \quad (5)$$

where the respective operators are:

$$\mathbf{L} = \begin{bmatrix} 0 & 0 & 0 \\ 1 & 0 & 0 \\ 0 & 0 & 0 \\ 0 & 0 & 0 \\ 0 & 0 & 0 \\ 0 & -1 & 0 \end{bmatrix}, \quad \mathbf{L}_r = \begin{bmatrix} 1 & 0 & 0 \\ 0 & 0 & 0 \\ 0 & 0 & 0 \\ 0 & 0 & 0 \\ 0 & 0 & 1 \\ 0 & 1 & 0 \end{bmatrix}, \quad \mathbf{L}_\theta = \begin{bmatrix} 0 & 0 & 0 \\ 0 & 1 & 0 \\ 0 & 0 & 0 \\ 0 & 0 & 1 \\ 0 & 0 & 0 \\ 1 & 0 & 0 \end{bmatrix}, \quad \mathbf{L}_z = \begin{bmatrix} 0 & 0 & 0 \\ 0 & 0 & 0 \\ 0 & 0 & 1 \\ 0 & 1 & 0 \\ 1 & 0 & 0 \\ 0 & 0 & 0 \end{bmatrix} \quad (6)$$

As in standard finite element procedures, the displacement within the element is approximated

using shape functions, such that

$$\bar{\mathbf{u}}(r, \theta, z, t) = \mathbf{N}(r)\bar{\mathbf{q}}(\theta, z, t) \quad (7)$$

where  $\bar{\mathbf{q}}(\theta, z, t)$  is a vector of nodal displacements. We can now rewrite Eq. (5) as

$$\bar{\boldsymbol{\varepsilon}} = \left( \frac{1}{r} \mathbf{L} \mathbf{N} + \mathbf{L}_r \mathbf{N}_{,r} + \frac{1}{r} \mathbf{L}_\theta \mathbf{N} \frac{\partial}{\partial \theta} + \mathbf{L}_z \mathbf{N} \frac{\partial}{\partial z} \right) \bar{\mathbf{q}} = \mathbf{B}_1 \bar{\mathbf{q}} + \mathbf{B}_2 \frac{\partial}{\partial \theta} \bar{\mathbf{q}} + \mathbf{B}_3 \frac{\partial}{\partial z} \bar{\mathbf{q}} \quad (8)$$

where  $\mathbf{N}_{,r}$  denotes a derivative with respect to  $r$  and the  $\mathbf{B}$  matrices are clearly defined in the last step.

Substituting Eq. (3) and Eq. (8) into Eq. (1), assuming time harmonic motion ( $\bar{\mathbf{q}} = \mathbf{q} e^{i\omega t}$ ) and noting that in the cylindrical coordinates  $dV = r dr d\theta dz$ , after multiple simplifications and integrations by parts, one obtains

$$\begin{aligned} & \int_L \int_\theta \delta \mathbf{q}^\top (-\omega^2 \mathbf{M} + \mathbf{K}_1 \mathbf{q} - \mathbf{K}_2 \mathbf{q}_{,\theta} - \mathbf{K}_3 \mathbf{q}_{,z} - \mathbf{K}_4 \mathbf{q}_{,z\theta} - \mathbf{K}_5 \mathbf{q}_{,\theta\theta} - \mathbf{K}_6 \mathbf{q}_{,zz}) d\theta dz + \\ & \int_\theta \delta \mathbf{q}^\top (\mathbf{K}_{f1}^\top \mathbf{q} + \mathbf{K}_{f3}^\top \mathbf{q}_{,\theta} + \mathbf{K}_6 \mathbf{q}_{,z}) d\theta + \int_L \delta \mathbf{q}^\top (\mathbf{K}_{f1} + \mathbf{K}_5 \mathbf{q}_{,\theta} + \mathbf{K}_{f3} \mathbf{q}_{,z}) dz = 0 \end{aligned} \quad (9)$$

where for convenience we used subscript notation to denote differentiation and the matrices have been integrated over the cross-section (with  $r_0$  and  $r_1$  being the start and end coordinates of the element) as follows

$$\begin{aligned} \mathbf{K}_1 &= 2\pi \int_{r_0}^{r_1} \mathbf{B}_1^\top \mathbf{C} \mathbf{B}_1 r dr & \mathbf{K}_{f1} &= 2\pi \int_{r_0}^{r_1} \mathbf{B}_1^\top \mathbf{C} \mathbf{B}_3 r dr \\ \mathbf{K}_{f2} &= 2\pi \int_{r_0}^{r_1} \mathbf{B}_1^\top \mathbf{C} \mathbf{B}_2 r dr & \mathbf{K}_{f3} &= 2\pi \int_{r_0}^{r_1} \mathbf{B}_2^\top \mathbf{C} \mathbf{B}_3 r dr \\ \mathbf{K}_2 &= \mathbf{K}_{f2}^\top - \mathbf{K}_{f2} & \mathbf{K}_3 &= \mathbf{K}_{f1}^\top - \mathbf{K}_{f1} \\ \mathbf{K}_4 &= \mathbf{K}_{f3}^\top + \mathbf{K}_{f3} & \mathbf{K}_5 &= 2\pi \int_{r_0}^{r_1} \mathbf{B}_2^\top \mathbf{C} \mathbf{B}_2 r dr \\ \mathbf{K}_6 &= 2\pi \int_{r_0}^{r_1} \mathbf{B}_3^\top \mathbf{C} \mathbf{B}_3 r dr & \mathbf{M} &= 2\pi \rho \int_{r_0}^{r_1} \mathbf{N}^\top \mathbf{N} r dr \end{aligned} \quad (10)$$

From Eq. (9) we can deduce the governing equation for wave propagation along  $z$ . Imposing the  $n$ -periodicity of the displacement along the circumference as indicated in Eq. (4) and assuming a spatially harmonic variation of the displacement along  $z$ , i.e.  $\mathbf{q}_n(z) = \tilde{\mathbf{q}}_n e^{-jkz}$ , we obtain

$$(\mathbf{K}_1 - \omega^2 \mathbf{M} + jn\mathbf{K}_2 + jk\mathbf{K}_3 + kn\mathbf{K}_4 + n^2\mathbf{K}_5 + k^2\mathbf{K}_6) \tilde{\mathbf{q}}_n = 0 \quad (11)$$

and the natural boundary condition for the waveguide (resultant forces over the cross-section)

$$(\mathbf{K}_{f1}^\top - jn\mathbf{K}_{f3}^\top - jk\mathbf{K}_6) \tilde{\mathbf{q}}_n = \tilde{\mathbf{f}}^z \quad (12)$$

It is noted that the considerations presented above address a one-dimensional waveguide problem. In this light, the cross-sectional integral in Eq. (12) is indeed a natural boundary condition.

## 2.2. Structure of the matrices

Matrices  $\mathbf{K}_1$ ,  $\mathbf{K}_4$ ,  $\mathbf{K}_5$ ,  $\mathbf{K}_6$  and  $\mathbf{M}$  are symmetric, whereas matrices  $\mathbf{K}_2$  and  $\mathbf{K}_3$  are skew-symmetric ( $\mathbf{K}_2 = -\mathbf{K}_2^\top$ ). The latter two matrices couple  $u_r$  with  $u_\theta$  and  $u_r$  with  $u_z$ , respectively. The forms of  $u_\theta$  and  $u_z$  are prescribed by the circumferential and axial periodicity, hence it is convenient to introduce a diagonal transformation matrix  $\mathbf{T}$  as proposed in [36]. The transformation matrix has the same dimension as the SAFE matrices and each diagonal element corresponding to  $u_r$  is 1, whereas elements corresponding to  $u_\theta$  and  $u_z$  are  $j$ . Eq. (11) is premultiplied by  $\mathbf{T}$  and  $\tilde{\mathbf{q}}$  is replaced by  $\mathbf{T}^*\mathbf{T}\tilde{\mathbf{q}}$ , since  $\mathbf{T}^*\mathbf{T} = \mathbf{I}$ , with  $\mathbf{T}^*$  being the conjugate of  $\mathbf{T}$ . Matrices  $\mathbf{K}_1$ ,  $\mathbf{K}_4$ ,  $\mathbf{K}_5$ ,  $\mathbf{K}_6$  and  $\mathbf{M}$  remain unaltered by this operation, whereas  $\mathbf{K}_2$  and  $\mathbf{K}_3$  become

$$\begin{aligned}\mathbf{TK}_2\mathbf{T}^* &= -j\hat{\mathbf{K}}_2 \\ \mathbf{TK}_3\mathbf{T}^* &= -j\hat{\mathbf{K}}_3\end{aligned}\tag{13}$$

where  $\hat{\mathbf{K}}_2$  and  $\hat{\mathbf{K}}_3$  are now symmetric. Eq. (11) can now be rewritten as

$$(\mathbf{K}_1 + n\hat{\mathbf{K}}_2 + n^2\mathbf{K}_5 - \omega^2\mathbf{M} + k(\hat{\mathbf{K}}_3 + n\mathbf{K}_4) + k^2\mathbf{K}_6)\mathbf{T}\tilde{\mathbf{q}} = 0\tag{14}$$

This transformation will not hold in the case of a general anisotropy, but can be applied to orthotropic and transversely isotropic materials, if the material axes are aligned with the cylindrical coordinate system adopted. For more general cases, the matrices are to be left in their original forms. Despite the loss of symmetry and its implications, the solution procedure outlined below is still the same.

## 2.3. Acoustic element

SAFE has typically been only used for solid structures. In this section, we derive an acoustic SAFE element to represent contained/surrounding fluids. We start from recalling the acoustic wave equation in terms of the velocity potential [37]

$$\nabla \cdot \nabla \phi - \frac{1}{c^2} \frac{\partial^2 \phi}{\partial t^2} = 0\tag{15}$$

where the gradient operator in cylindrical coordinates is defined as

$$\nabla X = \left[ \frac{\partial X}{\partial r} \quad \frac{1}{r} \frac{\partial X}{\partial \theta} \quad \frac{\partial X}{\partial z} \right]^\top\tag{16}$$

In Eq. (15),  $\phi$  is the velocity potential in the fluid and  $c$  is the speed of sound defined as

$$c = \sqrt{\frac{\beta}{\rho_f}}\tag{17}$$

with  $\beta$  being the bulk modulus and  $\rho_f$  – the mass density of the fluid. The velocity and pressure can be calculated from the potential as

$$\mathbf{v} = \nabla \phi \quad p = -\rho \frac{\partial \phi}{\partial t} \quad (18)$$

The virtual work principle for fluids states that [35]

$$\int_{V_f} \delta \phi \frac{1}{c^2} \frac{\partial^2 \phi}{\partial t^2} dV + \int_{V_f} (\nabla \delta \phi) \cdot (\nabla \phi) dV = 0 \quad (19)$$

where  $V_f$  is the volume occupied by the fluid. The velocity potential in the discretised medium is written as

$$\bar{\phi}(r, \theta, z, t) = \mathbf{N}_\phi(r) \boldsymbol{\phi}(z, \theta) e^{j\omega t} \quad (20)$$

where  $\mathbf{N}_\phi$  is the shape function matrix and  $\boldsymbol{\phi}$  is the nodal velocity potential vector. In this paper, the shape functions for  $\mathbf{N}_u$  and  $\mathbf{N}_\phi$  are the same. so that

$$\nabla \phi = \nabla [\mathbf{N}_\phi(r) \boldsymbol{\phi}(\theta, z)] = \left[ \mathbf{N}_{\phi,r} \boldsymbol{\phi} \quad \frac{1}{r} \mathbf{N}_\phi \frac{\partial}{\partial \theta} \boldsymbol{\phi} \quad \mathbf{N}_\phi \frac{\partial}{\partial z} \boldsymbol{\phi} \right] \quad (21)$$

where the time-harmonic factor has been omitted for brevity.

Let us now substitute the finite element approximations into the virtual work equation

$$\begin{aligned} & \frac{-\omega^2}{c^2} \int_{V_f} \delta \boldsymbol{\phi}^\top \mathbf{N}_\phi^\top \mathbf{N}_\phi \boldsymbol{\phi} dV + \int_{V_f} \delta \boldsymbol{\phi}^\top \mathbf{N}_{\phi,r}^\top \mathbf{N}_{\phi,r} \boldsymbol{\phi} dV \\ & \int_{V_f} \delta \frac{\partial}{\partial \theta} \boldsymbol{\phi}^\top \frac{1}{r^2} \mathbf{N}_\phi^\top \mathbf{N}_\phi \frac{\partial}{\partial \theta} \boldsymbol{\phi} dV + \\ & \int_{V_f} \delta \frac{\partial}{\partial z} \boldsymbol{\phi}^\top \mathbf{N}_\phi^\top \mathbf{N}_\phi \frac{\partial}{\partial z} \boldsymbol{\phi} dV = 0 \end{aligned} \quad (22)$$

After integrating the two last integrals by parts and noting that  $dV = r dr d\theta dz$ , we obtain

$$\begin{aligned} & \int_L \int_\theta \delta \boldsymbol{\phi}^\top \left( -\omega^2 \mathbf{M}^{\text{fluid}} \boldsymbol{\phi} + \mathbf{K}_1^{\text{fluid}} \boldsymbol{\phi} - \mathbf{K}_5^{\text{fluid}} \boldsymbol{\phi}_{,\theta\theta} - \mathbf{K}_6^{\text{fluid}} \boldsymbol{\phi}_{,zz} \right) d\theta dz + \\ & \int_\theta \delta \boldsymbol{\phi}^\top \mathbf{K}_6^{\text{fluid}} \boldsymbol{\phi}_{,z} d\theta + \int_L \delta \boldsymbol{\phi}^\top \mathbf{K}_5^{\text{fluid}} \boldsymbol{\phi}_{,\theta} dz = 0 \end{aligned} \quad (23)$$

where the respective matrices are defined as follows (to maintain consistency, we kept the same sub-



script notation as for the structural element)

$$\begin{aligned}
\mathbf{M}^{\text{fluid}} &= 2\pi \int_{r_0}^{r_1} \frac{1}{c^2} \mathbf{N}_\phi^\top \mathbf{N}_\phi r \, dr & \mathbf{K}_1^{\text{fluid}} &= 2\pi \int_{r_0}^{r_1} \mathbf{N}_{\phi,r}^\top \mathbf{N}_{\phi,r} r \, dr \\
\mathbf{K}_5^{\text{fluid}} &= 2\pi \int_{r_0}^{r_1} \frac{1}{r^2} \mathbf{N}_\phi^\top \mathbf{N}_\phi r \, dr & \mathbf{K}_6^{\text{fluid}} &= 2\pi \int_{r_0}^{r_1} \mathbf{N}_\phi^\top \mathbf{N}_\phi r \, dr
\end{aligned} \tag{24}$$

From Eq. (23) we can deduce the SAFE governing equation for wave propagation and the natural boundary condition (resultant pressure over the cross-section). Confining our attention to waves propagating along the  $z$  direction, we impose the circumferential periodicity condition from Eq. (4) and assume harmonic variation of the displacement along  $z$ , i.e.  $\phi_n(z) = \tilde{\phi}_n e^{-jkz}$ , to obtain

$$(\mathbf{K}_1^{\text{fluid}} - \omega^2 \mathbf{M}^{\text{fluid}} + n^2 \mathbf{K}_5^{\text{fluid}} + k^2 \mathbf{K}_6^{\text{fluid}}) \tilde{\phi}_n = \mathbf{0} \tag{25}$$

and

$$\tilde{\mathbf{p}} = (-jk \mathbf{K}_6^{\text{fluid}} - jn \mathbf{K}_5^{\text{fluid}}) \tilde{\phi}_n \tag{26}$$

For an acoustic problem, all matrices are symmetric and no transformation is required as in the case of structural elements. While applying the  $\mathbf{T}$  transformation to the global matrices of the assembled coupled fluid-solid problem, respective entries at the diagonal of  $\mathbf{T}$  corresponding to fluid velocity potential degrees of freedom are set to 1.

#### 2.4. Structural-acoustic coupling

Finally, in this section we derive structural-acoustic coupling relationships following the approach of Nilsson and Finnveden [38] who studied a fluid-filled pipe. We start from the virtual work principle for both the structural and acoustic part, including the interaction forces. For the former we have (assuming no external traction)

$$\int_{V_s} \delta \tilde{\mathbf{u}}^\top \rho_s \ddot{\tilde{\mathbf{u}}} \, dV + \int_{V_s} \delta \tilde{\boldsymbol{\epsilon}}^\top \tilde{\boldsymbol{\sigma}} \, dV = \int_S \delta \mathbf{n}^\top \mathbf{u} p \, dS \tag{27}$$

where  $\mathbf{n}$  is a vector normal to the wetted surface – in this case  $\mathbf{n} = [1 \ 0 \ 0]^\top$  and  $S$  is the wetted surface of contact between the structure and the fluid. The right hand side is virtual work done on the structure by the fluid pressure and it represents the coupling between the two media. In the above, the energy flow into the shell is defined positive [38]. Substituting the finite element approximations and noting that  $p = -\rho \dot{\phi}$  one writes

$$\int_S \delta \mathbf{n}^\top \mathbf{u} p \, dS = -j\omega\rho \int_S \delta \tilde{\mathbf{q}}^\top \mathbf{N}_u^\top \mathbf{n} \mathbf{N}_\phi \tilde{\phi} \, dS = -j\omega\rho \delta \tilde{\mathbf{q}}^\top \mathbf{H} \tilde{\phi} \tag{28}$$

where  $\mathbf{H} = \int_S \mathbf{N}_u^\top \mathbf{n} \mathbf{N}_\phi \, dS$  is defined in the last step.

Likewise, the virtual work principle for the acoustic part is written as

$$\int_{V_f} \delta \phi \frac{1}{c^2} \ddot{\phi} dV + \int_{V_f} (\nabla \delta \phi) \cdot (\nabla \phi) dV = - \int_S \delta p \mathbf{n}^\top \mathbf{u} dS \quad (29)$$

Here, the right-hand side is the virtual work done on the fluid by the structure and the minus sign originates from the chosen convention for the direction of energy flow. Employing finite element approximations, one obtains

$$- \int_S \delta p \mathbf{n}^\top \mathbf{u} dS = j\omega\rho \int_S \delta \tilde{\boldsymbol{\phi}}_i^\top \mathbf{N}_\phi^\top \mathbf{n}^\top \mathbf{N}_u \tilde{\mathbf{q}} dS = j\omega\rho \delta \tilde{\boldsymbol{\phi}}_i^\top \mathbf{H}^\top \tilde{\mathbf{q}} \quad (30)$$

Eq. (28) and Eq. (30) are the coupling terms which are the only modifications to the governing equations for the structural and acoustic parts derived above. It is noted that since  $\mathbf{H}$  couples  $\tilde{\boldsymbol{\phi}}_r$  with  $\tilde{\mathbf{q}}$ , it will only interact with the  $\mathbf{K}_1$  matrix. The coupling terms need to be formulated appropriately to the application, i.e. whether it is supposed to represent fluid contained within a structure (e.g. pipe), or a fluid surrounding a structure. The equations below refer to the former case.

Let us now write the governing equation for the assembly of structural and acoustic elements including the coupling term. Under the axisymmetric assumption, the wetted surface is represented by one node. The surface integral becomes

$$\int_S (\cdot) dS = \int_\theta (\cdot) r_s dS = 2\pi r_s (\cdot) \quad (31)$$

where  $r_s$  is the coordinate of the fluid-structure interface. The integral in the coupling term can be simplified to

$$\mathbf{H} = 2\pi r_s \mathbf{N}_u(r_s)^\top \mathbf{n} \mathbf{N}_\phi(r_s) \quad (32)$$

The assembly of a fluid and structural elements including the coupling is now written as

$$\left( -\omega^2 \begin{bmatrix} \mathbf{M}^{\text{fluid}} & \mathbf{0} \\ \mathbf{0} & \mathbf{M} \end{bmatrix} + \begin{bmatrix} \mathbf{K}_1^{\text{fluid}} + n^2 \mathbf{K}_5^{\text{fluid}} & \mathbf{0} \\ \mathbf{0} & \mathbf{K}_1 + n \hat{\mathbf{K}}_2 + n^2 \mathbf{K}_5 \end{bmatrix} + j\omega \begin{bmatrix} \mathbf{0} & \rho \mathbf{H}^\top \\ -\rho \mathbf{H} & \mathbf{0} \end{bmatrix} + \right. \\ \left. k \begin{bmatrix} \mathbf{0} & \mathbf{0} \\ \mathbf{0} & \hat{\mathbf{K}}_3 + n \mathbf{K}_4 \end{bmatrix} + k^2 \begin{bmatrix} \mathbf{K}_6^{\text{fluid}} & \mathbf{0} \\ \mathbf{0} & \mathbf{K}_6 \end{bmatrix} \right) \begin{Bmatrix} \tilde{\boldsymbol{\phi}} \\ \mathbf{T} \tilde{\mathbf{q}} \end{Bmatrix} = \mathbf{0} \quad (33)$$

where the ‘fluid’ superscript denotes that the matrix corresponds to the acoustic part of the structure. The symmetry is lost in the above problem, as the matrix with coupling terms is skew-symmetric. However, we can multiply the top row of the block matrix equation (corresponding to the fluid) by -1 to

obtain

$$\left( -\omega^2 \begin{bmatrix} -\mathbf{M}^{\text{fluid}} & \mathbf{0} \\ \mathbf{0} & \mathbf{M} \end{bmatrix} + \begin{bmatrix} -\mathbf{K}_1^{\text{fluid}} & -n^2 \mathbf{K}_5^{\text{fluid}} & \mathbf{0} \\ \mathbf{0} & \mathbf{0} & \mathbf{K}_1 + n\hat{\mathbf{K}}_2 + n^2 \mathbf{K}_5 \end{bmatrix} + j\omega \begin{bmatrix} \mathbf{0} & -\rho \mathbf{H}^\top \\ -\rho \mathbf{H} & \mathbf{0} \end{bmatrix} + k \begin{bmatrix} \mathbf{0} & \mathbf{0} \\ \mathbf{0} & \hat{\mathbf{K}}_3 + n\mathbf{K}_4 \end{bmatrix} + k^2 \begin{bmatrix} -\mathbf{K}_6^{\text{fluid}} & \mathbf{0} \\ \mathbf{0} & \mathbf{K}_6 \end{bmatrix} \right) \begin{Bmatrix} \check{\boldsymbol{\phi}} \\ \mathbf{T}\check{\mathbf{q}} \end{Bmatrix} = \mathbf{0} \quad (34)$$

where the symmetry is retained. For implementation, it is convenient to apply the ‘minus’ sign to all matrices related to the fluid domain at the element definition stage.

If the coupling between the pipe and the external surrounding fluid is considered, the rows of the matrices in Eq. (34) need to be swapped.

### 2.5. Spectral elements for the discretisation of the cross-section

The choice of shape functions is of primary importance for modelling wave propagation. Using high-order polynomials over non-uniformly spaced nodes, commonly referred to as spectral elements, offers several advantages over conventional finite elements with linear or quadratic interpolations [27, 39, 40]. These include fast convergence and reduced size of the model. They are particularly well suited to wave propagation problems, and hence were recently proposed for SAFE with 2D cross-sections [27]. The details of the implementation of spectral finite elements for the discretisation of the axisymmetric cross-section are discussed in this section.

#### 2.5.1. Gauss-Lobatto-Legendre nodes and Lagrangian interpolants

A detailed discussion on various interpolating polynomials and integration schemes can be found in relevant literature, e.g. [40]. In this paper, we use Lagrange polynomial shape functions over Gauss-Lobatto-Legendre (GLL) nodes. Unlike in the conventional FE, the nodes now coincide with the integration points.

Let us start from defining the nodal locations as roots of the equation [41]

$$(1 - \xi^2) \frac{dP_N(\xi)}{d\xi} = 0 \quad (35)$$

where  $P_N(\xi)$  is the Legendre polynomial of order  $N$ . These  $(N + 1)$  roots ( $\xi_i$ ) can be identified numerically. For completeness, the weights for the GLL quadrature are defined as:

$$w_i = \begin{cases} \frac{2}{N(N+1)} & \text{if } i = 0 \text{ or } i = N + 1 \\ \frac{2}{N(N+1)P_N(\xi_i)^2} & \text{otherwise} \end{cases} \quad (36)$$

For a given set of GLL nodes, we compute  $(N + 1)$  Lagrange interpolants of order  $N$ :

$$h_i(\xi) = \begin{cases} \prod_{j=1, i \neq j}^{N+1} \frac{\xi - \xi_j}{\xi_i - \xi_j} & \text{if } i \neq j \\ 1 & \text{otherwise} \end{cases} \quad (37)$$

The derivatives of the interpolants are calculated as:

$$\frac{dh_i(\xi)}{d\xi} = \sum_{j=1, i \neq j}^{N+1} \frac{1}{\xi_i - \xi_j} \prod_{k=1, k \neq (i,j)}^{N+1} \frac{\xi - \xi_k}{\xi_i - \xi_k} \quad (38)$$

For one-dimensional elements, the Jacobian matrix describing the mapping from physical into natural coordinates has just one element:

$$\mathbf{J} = \begin{bmatrix} \frac{dh_1}{d\xi} & \frac{dh_2}{d\xi} & \dots & \frac{dh_{N+1}}{d\xi} \end{bmatrix} \begin{bmatrix} r_1 & r_2 & \dots & r_{N+1} \end{bmatrix}^\top \quad (39)$$

The determinant of the Jacobian matrix is denoted as  $J$  ( $\det \mathbf{J} = J$ )

### 2.5.2. Gauss-Lobatto-Jacobi (0, 1) nodes and weights for core elements

For axisymmetric domains, adopting GLL nodal locations and integration results in the appearance of singular or undetermined terms at  $r = 0$  (every element matrix has the form  $\int \dots r dr$ ). Since GLL points include  $(-1, 1)$  coordinates, the element matrices need to be evaluated at  $r = 0$ , which corresponds to  $\xi = -1$  for the element adjacent to the axis of symmetry (core element).

Several approaches have been proposed to overcome this difficulty. In this paper we follow [42–45] who suggested employing the Gauss-Lobatto-Jacobi (0, 1) (GLJ) scheme for determining node locations and integrating over the core element. The advantage of the GLJ quadrature is that it incorporates the radius in the weight allowing for eliminating the aforementioned numerical difficulty. A brief summary of the calculation of nodes and weights for the GLJ quadrature is given in Appendix A. For detailed information, the reader is directed to literature related to spectral methods, e.g. [41].

### 2.5.3. Avoiding undetermined terms

The integrations of the axisymmetric element matrices can be written in a general form

$$\int_r f(r) r dr \quad (40)$$

Let us rewrite this integral in the natural coordinates (with respect to GLJ nodes)

$$\int_{-1}^1 f(\xi) \frac{r}{1 + \xi} (1 + \xi) J d\xi \quad (41)$$

where  $J$  is the determinant of the Jacobian matrix. The term  $(1 + \xi)$  is absorbed in the weight, since the GLJ quadrature is defined as

$$\int_{-1}^1 g(\xi)(1 + \xi) d\xi = \sum_{i=1}^{N+1} w_i g(\xi_i) \quad (42)$$

where  $\xi_i$  and  $w_i$  are GLJ nodes and weights, respectively. For the considered case  $g(\xi) = f(\xi)\frac{r}{1+\xi}$ . On the axis of symmetry, the  $\frac{r}{1+\xi}$  becomes undetermined since both  $r$  and  $(1 + \xi)$  tend to zero as  $\xi$  approaches  $-1$ . We evaluate this fraction using the L'Hospital's rule [42]

$$\left. \frac{r(\xi)}{1 + \xi} \right|_{\xi=-1} = \left. \frac{dr}{d\xi} \right|_{\xi=-1} \quad (43)$$

From the finite element discretisation,  $r(\xi) = \mathbf{N}(\xi)\mathbf{r}_i$ , where  $\mathbf{r}_i$  are  $r$ -coordinates of the nodes. Therefore,

$$\left. \frac{dr}{d\xi} \right|_{\xi=-1} = \left. \frac{d\mathbf{N}(\xi)}{d\xi} \right|_{\xi=-1} \mathbf{r}_i \quad (44)$$

which is equal to the one-element Jacobian matrix.

For implementation, it is convenient to scale the radius for core elements according to the node at which the matrices are evaluated [42]

$$r = \begin{cases} \frac{r}{1 + \xi} & \text{if } \xi \neq -1 \\ J & \text{if } \xi = -1 \end{cases} \quad (45)$$

Another singularity arises when strains in a solid domain are computed on the axis of symmetry. In cylindrical coordinates, several components include division by  $r$ , for example  $u_r/r$ , or  $u_\theta/r$  (for  $n = 0$  circumferential order). We note, however that the boundary conditions on the axis of symmetry imply that both  $u_r$  and  $u_\theta$  vanish. The L'Hospital's rule can be applied again [45]

$$\left. \frac{u_r}{r} \right|_{\xi=-1} = \left[ \left. \frac{dr}{d\xi} \right|_{\xi=-1} \right]^{-1} \left. \frac{du_r}{d\xi} \right|_{\xi=-1} \quad (46)$$

where the  $z$ - and  $\theta$ - dependence of the displacement has been dropped. Recalling that  $u_r(\xi) = \mathbf{N}(\xi)\mathbf{u}_{r_i}$  we can write the derivative of the displacement as

$$\frac{du_r}{d\xi} = J\mathbf{N}_{,r}\mathbf{u}_{r_i} \quad (47)$$

which finally yields

$$\left. \frac{u_r}{r} \right|_{\xi=-1} = \mathbf{N}_{,r} \Big|_{\xi=-1} \mathbf{u}_{r_i} \quad (48)$$

An analogous derivation applies to the  $\frac{u_\theta}{r}$  component and all derivatives over  $\theta$ . Recalling Eq. (8),

where the FE formulation for strain was derived, we redefine strain for  $\xi = -1$  the node in the core element located at the axis of symmetry as

$$\bar{\epsilon} \Big|_{\xi=-1} = \left( \mathbf{L}\mathbf{N}_{,r} + \mathbf{L}_r\mathbf{N}_{,r} + \mathbf{L}_\theta\mathbf{N}_{,r} \frac{\partial}{\partial \theta} + \mathbf{L}_z\mathbf{N} \frac{\partial}{\partial z} \right) \bar{\mathbf{q}} \quad (49)$$

The aforementioned solutions allow for avoiding singular and undetermined terms in element matrices making the use of spectral elements in axisymmetric domains feasible.

### 3. Perfectly matched layer in SAFE

In this section the implementation of a perfectly matched layer (PML) in SAFE is presented. PMLs are of great use for modelling waves in structures embedded in a restraining medium. PML maps the original geometry into a new coordinate system which both ‘stretches’ the original geometry and attenuates the waves (as the new coordinate is complex). The new coordinate  $\tilde{r}(r)$  is defined as

$$\tilde{r}(r) = \int_0^r \gamma(\xi) d\xi \quad (50)$$

where  $\gamma$  is a stretching function defining the PML profile.

There are a number of variants to choose for the  $\gamma$  function. Two have received attention in the vibroacoustic community, namely a polynomial [25–27] and an exponential [28] profile. The latter seems to align better with the physical intuition and according to [28] outperforms the polynomial counterpart for most cases. The exponential profile is defined as

$$\gamma(r) = \begin{cases} 1 & r \leq d \\ e^{a\frac{r-d}{h}} - j \left( e^{b\frac{r-d}{h}} - 1 \right) & r > d \end{cases} \quad (51)$$

where  $a$  and  $b$  are the parameters of the profile. An average value of of the PML profile along its length provides a useful measure for evaluating its characteristics and will be exploited for determining the parameters of the PML.

$$\hat{\gamma} = \frac{1}{h} \int_d^{d+h} \gamma(r) dr = \frac{e^a - 1}{a} + j \frac{b - e^b + 1}{b} \quad (52)$$

The transformed stretched coordinate can be found from a closed-form expression:

$$\tilde{r}(r_i) = \int_0^{r_i} \gamma(\xi) d\xi = d + \frac{h}{a} \left( e^{a\frac{r_i-d}{h}} - 1 \right) - jh \left( \frac{1}{b} e^{b\frac{r_i-d}{h}} - \frac{1}{b} - r_i \right) \quad (53)$$

The SAFE-PML elements are derived in the same way as the ‘standard’ elements described in Sec. 2.1 and Sec. 2.3, the only difference being that the calculations are performed in the new, ‘stretched’ domain. Below, we show the modifications to element matrices for PML elements. The change of variables

$\tilde{r} \mapsto r$  implies that for any function  $\tilde{f}$

$$\frac{\partial \tilde{f}}{\partial \tilde{r}} = \frac{1}{\gamma} \frac{\partial f}{\partial r}, \quad d\tilde{r} = \gamma dr \quad (54)$$

In fact, this transformation is the only change to the SAFE matrices derived in the preceding sections. Both the form of the SAFE governing equation and the global matrices assembly process remain the same as for elements in physical coordinates. Nevertheless, the respective element matrices are written explicitly below, for completeness.

For structural elements, we obtain

$$\begin{aligned} \mathbf{K}_1 &= 2\pi \int_{r_0}^{r_1} \tilde{\mathbf{B}}_1^\top \mathbf{C} \tilde{\mathbf{B}}_1 \tilde{r} \gamma \, dr & \mathbf{K}_{f1} &= 2\pi \int_{r_0}^{r_1} \mathbf{B}_1^\top \mathbf{C} \tilde{\mathbf{B}}_3 \tilde{r} \gamma \, dr \\ \mathbf{K}_{f2} &= 2\pi \int_{r_0}^{r_1} \tilde{\mathbf{B}}_1^\top \mathbf{C} \tilde{\mathbf{B}}_2 \tilde{r} \gamma \, dr & \mathbf{K}_{f3} &= 2\pi \int_{r_0}^{r_1} \tilde{\mathbf{B}}_2^\top \mathbf{C} \tilde{\mathbf{B}}_3 \tilde{r} \gamma \, dr \\ \mathbf{K}_2 &= \mathbf{K}_{f2}^\top - \mathbf{K}_{f2} & \mathbf{K}_3 &= \mathbf{K}_{f1}^\top - \mathbf{K}_{f1} \\ \mathbf{K}_4 &= \mathbf{K}_{f3}^\top + \mathbf{K}_{f3} & \mathbf{K}_5 &= 2\pi \int_{r_0}^{r_1} \tilde{\mathbf{B}}_2^\top \mathbf{C} \tilde{\mathbf{B}}_2 \tilde{r} \gamma \, dr \\ \mathbf{K}_6 &= 2\pi \int_{r_0}^{r_1} \mathbf{B}_3^\top \mathbf{C} \tilde{\mathbf{B}}_3 \tilde{r} \gamma \, dr & \mathbf{M} &= 2\pi \rho \int_{r_0}^{r_1} \mathbf{N}^\top \mathbf{N} \tilde{r} \gamma \, dr \end{aligned} \quad (55)$$

with

$$\tilde{\mathbf{B}}_1 = \frac{1}{\tilde{r}} \mathbf{L} \mathbf{N} + \frac{1}{\gamma(r)} \mathbf{L}_r \mathbf{N}_{,r} \quad \text{and} \quad \tilde{\mathbf{B}}_2 = \frac{1}{\tilde{r}} \mathbf{L}_\theta \mathbf{N} \quad (56)$$

For acoustic elements, we write

$$\begin{aligned} \mathbf{M}^{\text{fluid}} &= \int_{r_0}^{r_1} \frac{1}{c^2} \mathbf{N}_\phi^\top \mathbf{N}_\phi \gamma \tilde{r} \, dr & \mathbf{K}_1^{\text{fluid}} &= \int_{r_0}^{r_1} \frac{1}{\gamma^2} \mathbf{N}_{\phi,r}^\top \mathbf{N}_{\phi,r} \gamma \tilde{r} \, dr \\ \mathbf{K}_5^{\text{fluid}} &= \int_{r_0}^{r_1} \frac{1}{\tilde{r}^2} \mathbf{N}_\phi^\top \mathbf{N}_\phi \gamma \tilde{r} \, dr & \mathbf{K}_6^{\text{fluid}} &= \int_{r_0}^{r_1} \mathbf{N}_\phi^\top \mathbf{N}_\phi \gamma \tilde{r} \, dr \end{aligned} \quad (57)$$

When calculating the integrals using the Gauss quadrature, both the stretching function  $\gamma$  and the transformed coordinate  $\tilde{r}$  are evaluated at each integration point.

### 3.1. The choice of the parameters of the PML and meshing

The physical implications of the geometrical parameters of the PML as well as the average value of the stretching function  $\hat{\gamma}(r)$  are explained in detail in excellent discussions by Treyssède [25] and Nguyen et al. [26]. Based on their observations, we formulated several criteria that allow for determining a practical rule for the choice of the parameters of the PML for a given configuration *a priori*,

minimising the need for manual tuning. In the following, the PML always starts at the boundary between the waveguide and the surrounding medium (preventing the growth of the leaky waves [26]).

In general, two limiting cases define the effectiveness of the PML, namely the long wavelength and the short wavelength limits. In the former, the challenge is to capture leaky waves when the wavelength in the surrounding medium is long and it is difficult to achieve attenuation with reasonably thin PMLs. The latter requires a careful consideration of the mesh density as one of the effects of the PML is to shorten the wavelength.

The short wavelength limit is addressed first. We start from computing the ‘largest’ radial wavenumber, which can be done from bulk wavenumbers in the waveguide ( $k_w$ ) and in the surrounding medium ( $k_b$ ) and the maximum allowed radial attenuation (expressed with the imaginary part of the radial wavenumber  $k_{\text{im max}}$  - to be chosen by the modeller)

$$k_{r \text{ max}} = \sqrt{\text{Re}(k_b)^2 - \text{Re}(k_w)^2} - jk_{\text{im max}} \quad (58)$$

It is noted that such calculation can be performed a priori, using the material properties and the frequency only. This is based on the fact, that the leaky wave wavenumber will not be smaller than the shear bulk wavenumber in the waveguide. For solid media, where two bulk waves exist (shear and longitudinal), a combination that gives the largest radial wavenumber must be chosen. The value taken for the maximum allowed radial attenuation should be relatively small (e.g. up to 10) to maintain relevance to practical guided wave problems.

Next, the effect of the PML on the wavelength is assessed. The exponential PML profile from Eq. (51) is controlled by two parameters:  $a$ , which is predominantly responsible for shortening the wavelength, and  $b$  which governs attenuation. The choice of values for these is somewhat arbitrary, but the experience of the authors shows that it is best if  $b$  is slightly larger than  $a$  and that a reasonable range for these parameters is between 2 and 8. The chosen profile performs very well for  $a = 6$  and  $b = 7$  and these values were kept for all simulations.

Having chosen  $a$  and  $b$ , one can calculate the ‘shortened’ wavelength in the PML. Recalling the harmonic variation of displacement along  $r$ ,  $e^{-jk_r r}$ , the effective PML wavenumber is obtained by substituting the maximum wavenumber  $k_{r \text{ max}}$  and the stretched radial coordinate from Eq. (53) to that expression. The wavelength is the shortest at the end of the PML ( $r = d + h$ ), hence one writes

$$e^{-jk_{r \text{ max}} \tilde{r}(r)} \Big|_{r=(d+h)} = e^{-j[\text{Re}(k_{r \text{ max}}) + j\text{Im}(k_{r \text{ max}})] \left[ d + \frac{h}{a}(e^a - 1) - j\left(\frac{h}{b}(e^b - 1)\right) + jh \right]} \quad (59)$$

The above equation can be mapped to the form  $e^{-jk_{\text{PML}} r} \Big|_{r=(d+h)}$  which allows for determining the effective PML wavenumber ( $k_{\text{PML}}$ ) at the PML termination. Although the full expression is rather lengthy, it can be well approximated with just one term (see Appendix B for the details of the approximation)

$$k_{\text{PML}} \approx \frac{h}{d+h} k_{r \text{ max}} \frac{e^a - 1}{a} \quad (60)$$



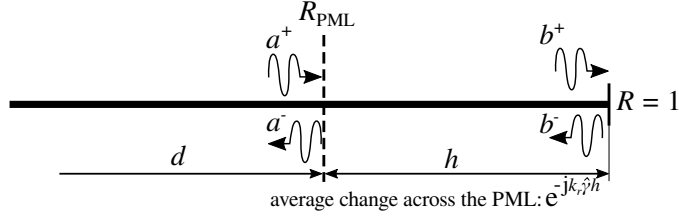


Figure 2: Schematic diagram for the calculation of the PML reflection coefficient  $R_{\text{PML}}$ .

This approximation is valid for most leaky waves cases, where the bulk waves in the waveguide are significantly faster than those in the surrounding medium and the bulk attenuation is relatively small.

Next, it is necessary to specify the number of ‘shortened’ wavelengths inside the PML. The experience suggests that somewhere between 3 and 10 both provides accurate results and avoids incurring excessive computational costs. A small number of wavelengths will suffice for most applications with high contrast of acoustic impedances between the waveguide and the surrounding medium. If the acoustic impedances are similar, and highly damped leaky waves are of interest, one should choose a value closer to ten. It is worth noting that choosing a larger number enhances the performance of the PML at lower frequencies.

Knowing the smallest shortened wavelength in the PML, its physical thickness can be calculated from a simple quadratic equation

$$\kappa \frac{2\pi}{k_{\text{PML}}} = h \quad (61)$$

where  $\kappa$  is the desired number of wavelengths and  $k_{\text{PML}}$  is taken from Eq. (60).

At high frequencies, the mesh density becomes critical for reflection-free performance of the PML. A criterion developed by Gravenkamp [30] is adopted here, with slight reformulations. Recalling that it has been chosen to include  $\kappa$  wavelengths within the PML, the order of the GLL element ( $N$ ) should be

$$N = \pi\kappa + 3 \quad (62)$$

which gives an element with  $N + 1$  nodes.

The equations presented above allow for determining the thickness of the PML and mesh parameters only from the geometry of the waveguide and material properties.

A very advantageous characteristic of the presented formulation is that it is capable of capturing leaky waves at very low frequencies, i.e. where the wavelengths in the surrounding medium are long. This is uncommon for PML applications. Most other numerical methods for embedded waveguides discussed in the introduction (see e.g. [19]) do not address the low frequency range. We found that the most practical is to calculate PML parameters for the short wavelength limit, evaluate the performance of the PML at the long wavelength limit and make small adjustments if necessary. This can be done by calculating the reflection coefficient from the PML at low frequencies. A schematic diagram for this calculation is shown in Fig. 2. We assume that the reflection coefficient at the end of the PML is 1 (one

wave type at a time, no mode conversion). Wave amplitude returning from the PML into the waveguide can be calculated as

$$a^- = a^+ e^{-2jk_r \hat{\gamma} h} \quad (63)$$

and the reflection coefficient from the PML as

$$R_{\text{PML}} = \frac{a^-}{a^+} = e^{-2jk_r \hat{\gamma} h} \quad (64)$$

Of interest here is the magnitude of the reflection coefficient, which can be conveniently expressed as

$$|R_{\text{PML}}| = e^{\text{Im}(2k_r \hat{\gamma} h)} \quad (65)$$

Substituting Eq. (52) from  $\hat{\gamma}$  we obtain

$$|R_{\text{PML}}| = e^{2h \text{Im}(k_r) \frac{e^a - 1}{a}} e^{2h \text{Re}(k_r) \frac{b - e^b + 1}{b}} \quad (66)$$

We calculated the reflection coefficients for several configurations and concluded that the exponential PMLs optimised for high frequency applications often work at low frequencies if at least three shortened wavelengths are included. If the dispersion curves become affected by the reflections from the PML at low frequencies, it is advised to increase  $\kappa$ .

Recent literature offers some promising approaches for formulating PMLs that are optimal in the sense that all incoming waves are fully absorbed, regardless of the angle of incidence. Bermudez et al. [46] proposed using unbounded absorbing functions for acoustic problems and developed optimal profile parameters ensuring perfect absorption. Follow-up considerations for a parameter-free formulation were also presented in [47]. Angle of incidence does not pose an issue for the problem considered in this paper. However, a comparison between the presented approach and rigorously optimised techniques from [46, 47] is an interesting topic for future work on SAFE-PML modelling.

## 4. Governing equations and solution

### 4.1. Linearisation and solution

The global SAFE matrices are assembled from element matrices defined in Sec. 2 in an FE-like manner, and coupling terms are grouped in  $\underline{\mathbf{K}}_{\text{coupling}}$ . The resulting governing equation is

$$\left( \underline{\mathbf{K}}_1 + n \hat{\underline{\mathbf{K}}}_2 + n^2 \underline{\mathbf{K}}_5 - \omega^2 \underline{\mathbf{M}} + j\omega \underline{\mathbf{K}}_{\text{coupling}} + k \left( \hat{\underline{\mathbf{K}}}_3 + n \underline{\mathbf{K}}_4 \right) + k^2 \underline{\mathbf{K}}_6 \right) \boldsymbol{\psi} = 0 \quad (67)$$

where  $\boldsymbol{\psi}$  is a  $\mathbf{T}$ -transformed vector of generalised nodal degrees of freedom (here, both displacements and velocity potentials).

Eq. (67) can be solved at a given frequency by companion linearisation (recasting to the form  $[\mathbf{A} - k\mathbf{B}]\hat{\boldsymbol{\psi}} = \mathbf{0}$ ). From a variety of linearisation schemes available, we chose one that allows for the

symmetry of the system to be retained and renders  $\mathbf{B}$  matrix invertible, namely

$$\left( \begin{bmatrix} \underline{\mathbf{K}}_6 & \mathbf{0} \\ \mathbf{0} & -(\underline{\mathbf{K}}_1 + n\underline{\hat{\mathbf{K}}}_2 + n^2\underline{\mathbf{K}}_5 - \omega^2\underline{\mathbf{M}} + j\omega\underline{\mathbf{K}}_{\text{coupling}}) \end{bmatrix} - k \begin{bmatrix} \mathbf{0} & \underline{\mathbf{K}}_6 \\ \underline{\mathbf{K}}_6 & \underline{\hat{\mathbf{K}}}_3 + n\underline{\mathbf{K}}_4 \end{bmatrix} \right) \begin{Bmatrix} k\psi \\ \psi \end{Bmatrix} = \mathbf{0} \quad (68)$$

The solutions of Eq. (68) can be efficiently found by transforming the above equation to a standard eigenvalue problem  $(\mathbf{B}^{-1}\mathbf{A} - k\mathbf{I})\hat{\psi} = \mathbf{0}$ , with  $\mathbf{A}$  and  $\mathbf{B}$  being the two block matrices in Eq. (68). Note that  $\mathbf{B}^{-1}$  needs to be computed only once, as it is independent of frequency. The structure of the matrices enables the shift-invert mode of sparse eigensolvers to be used. However, the axisymmetric assumption and the use of spectral elements usually render small problems, for which the full eigensolution is more efficient. Finally, owing to the symmetry of the system resulting from the  $\mathbf{T}$ -transformation outlined in Sec. 2.2, left eigenvectors are the same as the right eigenvectors, which is useful for calculating the real reciprocity relation [48] or the forced response. For generally anisotropic materials, one needs to find left eigenvectors separately, since without the  $\mathbf{T}$ -transformation, the system is not symmetric.

The solution of Eq. (68) yields  $2N$  eigenvalues and  $2N$  eigenvectors (with  $N$  being the number of degrees of freedom) corresponding to  $N$  positive- and  $N$  negative-going wavenumbers and wave mode shapes, respectively (if the full solution is used). The eigenvector can be transformed back to the physical space by premultiplying by  $\mathbf{T}^*$  (see Sec. 2.2). Positive-going waves are identified by verifying whether  $|e^{-jk\Delta}|$  is smaller than one (with  $\Delta$  being a small distance as compared to the wavelength) or, in case it is equal to one, whether the wave has a positive average power flow. In most cases, only positive-going waves are of interest.

SAFE formulation provides elegant expressions for a number of quantities of interest for guided wave problems. The time-averaged kinetic energy for wave  $i$  can be calculated as

$$E_{k,i} = \frac{\omega^2}{4} [\mathbf{T}^*\psi_i]^*{}^\top \underline{\mathbf{M}} \mathbf{T}^*\psi_i \quad (69)$$

The time-averaged potential energy can be obtained from

$$E_{p,i} = \frac{1}{4} [\mathbf{T}^*\psi_i]^*{}^\top \left( \underline{\mathbf{K}}_1 + jn\underline{\mathbf{K}}_2 + n^2\underline{\mathbf{K}}_5 + jk_i^*\underline{\mathbf{K}}_F - jk_i\underline{\mathbf{K}}_F^\top + k_i n\underline{\mathbf{K}}_{Ft}^\top + k_i^* n\underline{\mathbf{K}}_{Ft} + k_i k_i^* \underline{\mathbf{K}}_6 \right) \mathbf{T}^*\psi_i \quad (70)$$

The component of the Poynting vector along the direction of propagation, corresponding to the power flow density, is evaluated from

$$P_i = \frac{-\omega}{2} \text{Im} \left( [\mathbf{T}^*\psi_i]^*{}^\top (\underline{\mathbf{K}}_F - jn\underline{\mathbf{K}}_{Ft} - jk_i\underline{\mathbf{K}}_6) \mathbf{T}^*\psi_i \right) \quad (71)$$

And finally, the energy velocity can be calculated using the above mentioned quantities as:

$$c_{E,i} = \frac{P_i}{E_{p,i} + E_{k,i}} \quad (72)$$

For embedded waveguides, the energies, power and energy velocity are calculated from the subvectors and submatrices corresponding to the degrees of freedom of the core waveguide only.

#### 4.2. Mode sorting

The numerical eigenvalue routine used to solve the SAFE governing equation returns the solutions unordered and any physical interpretation must be preceded by some kind of sorting routine. The most straightforward approach is to use the biorthogonality relation

$$\hat{\mathbf{v}}_i^\top \mathbf{B} \hat{\boldsymbol{\psi}}_j = b_j \delta_{ij} \quad (73)$$

where  $\hat{\mathbf{v}}_i$  is the left eigenvector of Eq. (68), which for the considered problem is the same as the right eigenvector,  $\hat{\boldsymbol{\psi}}_i$ . Calculating Eq. (73) at two adjacent frequencies allows for determining the similarity between particular wave solutions. It is convenient to normalise the eigenvectors with respect to Eq. (73) after the eigensolution and before mode sorting. Any two eigenvectors at neighbouring frequencies for which  $\hat{\boldsymbol{\psi}}_i^\top(\omega_{i-1}) \mathbf{B} \hat{\boldsymbol{\psi}}_j(\omega_i)$  is one, or close to one, correspond to the same dispersion curve.

SAFE models typically return a large number of wave solutions, of which only a small number corresponds to propagating waves. Moreover, for embedded waveguides, one needs to discern between guided waves and radiation waves (oscillating within the PML), which are of no interest. For the former, an arbitrary maximum allowable attenuation can be set corresponding to the application of interest. The latter can be achieved using an energy criterion as proposed in [25], where a ratio between kinetic energies in the PML and the whole waveguide was used to calculate an energy ratio

$$\eta = \frac{|E_{\text{PML}}|}{|E_{\text{total}}|} \quad (74)$$

where the magnitudes have been taken as the energies are complex in the stretched domain. The value of  $\eta$  is set arbitrarily, most often around 0.9 [26, 28].

### 5. Numerical verification – high frequency

In this section we validate the formulation developed in this paper with results from published literature. The purpose of the comparison is to demonstrate the accuracy and efficiency of the proposed approach. Three high frequency (ultrasonic range) cases have been chosen from the literature: (i) a circular steel rod in concrete [19, 26, 28], (ii) titanium rod in oil [32] and water-filled copper pipe in water [49]. All computations are performed on a personal laptop (Intel Core i5-3340M CPU @ 2.70GHz  $\times$  4, 15.6 GB RAM) using an implementation of the presented method in Python/SciPy/NumPy (SciPy is based on LAPACK routines for linear algebra). It is noted that the inversion of  $\mathbf{B}$  mentioned in Sec. 4.1 is performed only once for each case. Owing to the circumferential periodicity assumption and the use of spectral elements, problem sizes are rather small and this inversion takes negligible time as compared to the eigensolution.

Table 1: Material properties and geometrical parameters for the steel rod in concrete case study (taken from [19])

| material | $c_L$ , km/s | $c_S$ , km/s | $\rho$ , kg m <sup>-3</sup> |
|----------|--------------|--------------|-----------------------------|
| steel    | 5960         | 3260         | 7932                        |
| concrete | 4222.1       | 2637.5       | 2300                        |

For all cases, the thicknesses and element orders for the PMLs were chosen according to criteria presented in Sec. 3.1. For structural layers, the order of the spectral elements was chosen based on the criterion adopted from [30]:

$$N = \pi \frac{h}{\lambda_{\min}} + 3 \quad (75)$$

where  $N$  is the element order,  $h$  is the thickness of the layer and  $\lambda_{\min}$  is the shortest bulk wavelength in the frequency range of interest.

### 5.1. Steel rod in concrete

A circular steel rod with 0.01 m radius embedded in concrete is considered first. No fluid is present in this scenario but it is used to validate the implementation of spectral elements and the choice of PML parameters. This configuration has been studied by a number of researchers to date, two of which [26, 28] employed perfectly matched layers with SAFE. The PML was set to start at the interface between the rod and the concrete ( $d = 0.01$  m) and respective material properties are given in Tab. 1. According to the criteria presented in Sec. 3.1, the PML thickness was set to 0.0043 m and meshed with an element of order 22, which allowed for including six shortened PML wavelengths at the highest frequency of interest with  $a = 6$  and  $b = 7$ . The results are presented in Fig. 3 and with regard to the results from the aforementioned references, they show excellent agreement. Some lines are discontinuous or do not cover the same range of frequencies owing to different conditions on identifying leaky waves.

One characteristic feature pointed out by the aforementioned authors is the discontinuity of  $L(0, 1)$  and  $F(2, 1)$  dispersion curves around the apparent crossing with longitudinal bulk wavespeed in concrete. This phenomenon is attributed to a change in the leakage pattern when the longitudinal waves cease to be radiated, owing to the Snell's law. It is worth noting that computing the solution at a single frequency step (including sorting of the waves) took around 36.8 ms on a personal laptop (as compared to 1.31 s reported in [28]), and that inversion of  $\mathbf{B}$  took 2 ms.

The benefits of using spectral elements become more evident if large problems are considered. In SAFE, significant savings are expected for 2D cross-sections, as recently proposed in [27]. However, this example shows that even for one-dimensional meshes the computational time is reduced of well more than an order of magnitude owing to the use of spectral elements.

### 5.2. Titanium rod in oil

The second example, titanium rod in oil as considered by Granvenkamp et al. [32], allows for demonstrating the structural-acoustic coupling implemented in the presented formulation. A circular

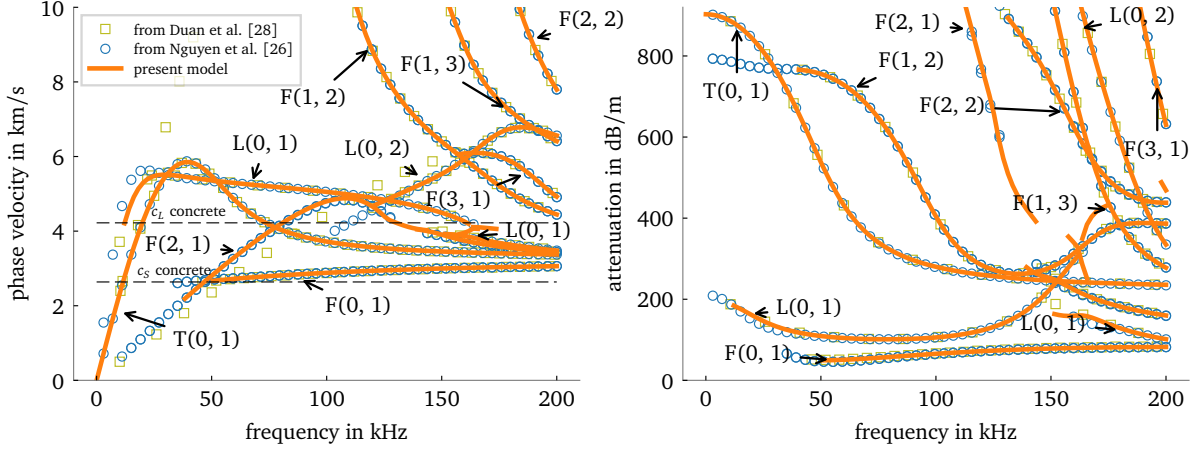


Figure 3: Phase velocity and attenuation for a steel rod embedded in concrete (the first three circumferential orders): a comparison with data from [26] and digitised data from [28]; present model results cover waves with  $\eta < 0.9$  and  $|\text{Im}(k)| < 200$ .

Table 2: Material properties and geometrical parameters for the titanium rod in oil case study (taken from [32])

| material | $c_L$ , km/s | $c_S$ , km/s | $\rho$ , kg m <sup>-3</sup> |
|----------|--------------|--------------|-----------------------------|
| titanium | 6064.5       | 3230         | 4460                        |
| oil      | 1740         | -            | 870                         |

rod of radius 1 mm is embedded in oil (material properties given in Tab. 2). As before, the PML is set to start at the boundary between the two materials and its thickness is calculated at 0.2 mm (the order of the PML spectral element is 13). The results are presented in Fig. 4 and, again, are found to be in very good agreement with data from [32]. The solution time for one frequency step (including wave sorting) was 9.1 ms.

### 5.3. Water-filled copper pipe submerged in water

The final numerical example is inspired by [49], who considered waves in a water-filled copper pipe with inner radius of 6.8 mm and wall thickness 0.7 mm. Material properties are given in Tab. 3. The PML was set to start at the boundary between the two materials, had thickness of 2.1 mm and was meshed with a spectral element of order 29. The solution time for one frequency step, including wave sorting was 17.4 ms. The results shown in Fig. 5 are in very good agreement data digitised from [49].

The fluid-dominated wave has nearly zero attenuation, unlike other identified solutions. One may notice small oscillations on the attenuation curve for the fluid-dominated wave between 0.06 and 0.1 MHz, where the group velocity drops. Within this frequency range, the displacement decays in the PML so rapidly that it requires high-order meshing. Increasing the number of desired ‘shortened’ PML wavelengths (see Sec. 3.1) helps to obtain more effective parameters for the PML (here,  $c = 8$  was used).

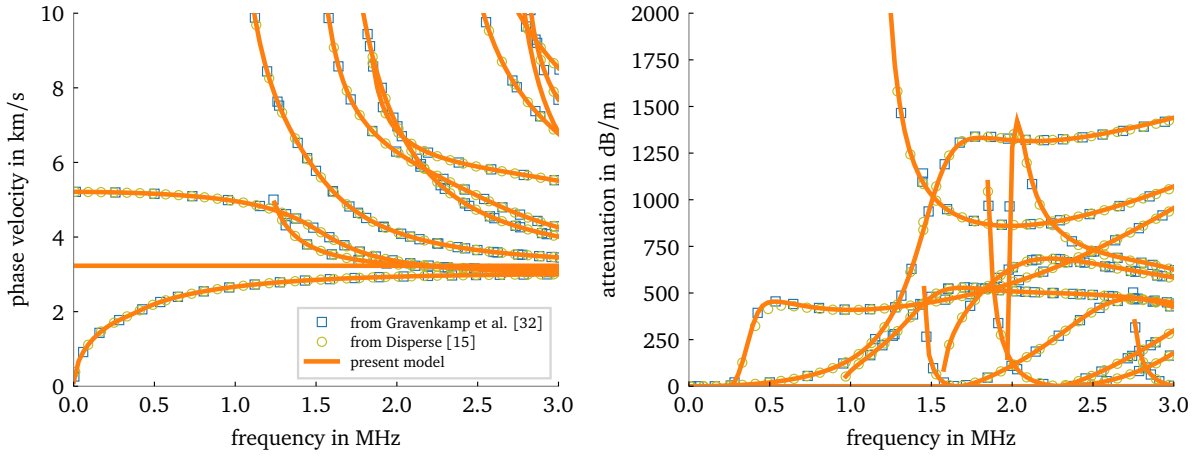


Figure 4: Phase velocity and attenuation for a titanium rod submerged in motor oil (the first three circumferential orders): a comparison with data from [32]; present model results cover waves with  $\eta < 0.97$  and  $|\text{Im}(k)| < 350$ .

Table 3: Material properties and geometrical parameters for the water-filled copper pipe in water case study (taken from [49])

| material | $c_L$ , km/s | $c_S$ , km/s | $\rho$ , kg m <sup>-3</sup> |
|----------|--------------|--------------|-----------------------------|
| copper   | 4759         | 2325         | 8933                        |
| water    | 1500         | -            | 1000                        |

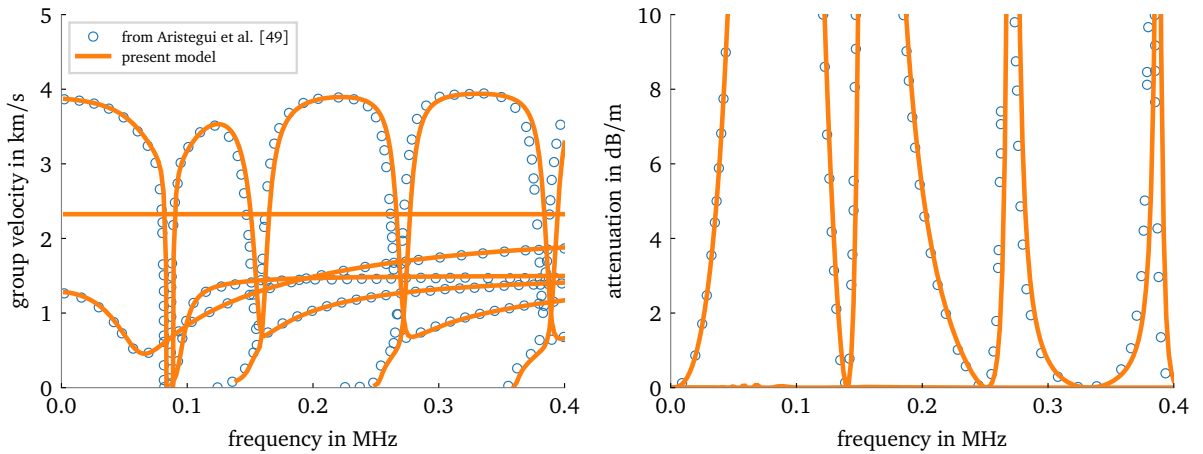


Figure 5: Group velocity and attenuation for a water-filled copper pipe submerged in water ( $n = 0$ ): a comparison with digitised data from [49]; present model results cover waves with  $\eta < 0.9$  and  $|\text{Im}(k)| < 100$ .

Table 4: Material properties and geometrical parameters for the water-filled, buried MDPE pipe case study (taken from [9])

| material   | $c_L$ , km/s | $c_S$ , km/s | $\rho$ , kg m <sup>-3</sup> | loss factor |
|------------|--------------|--------------|-----------------------------|-------------|
| MDPE       | 2182.2       | 890.9        | 900                         | 0.06        |
| sandy soil | 200          | 100          | 1500                        | -           |
| water      | 1500         | -            | 1000                        | -           |

## 6. Experimental validation – low frequency

In this section we validate the developed model against low frequency (audible frequency range) measurements on a buried and a submerged water-filled plastic pipe. The low frequency regime is particularly challenging from the viewpoint of PMLs and although not very popular for non-destructive testing, it has demonstrated a strong potential for successful mapping and assessment of buried water pipes [50, 51].

### 6.1. Water-filled buried plastic pipe

We consider an MDPE pipe with the inner radius of 0.079 m and wall thickness 0.011 m. The pipe is filled with water and buried in a sandy soil at a depth of approximately 1 m. Respective material properties are given in Tab. 4. Experimental wavenumbers are estimated from a number of hydrophones installed along the pipe. For the details of the experimental setup and data processing, the reader is referred to [9]. We note that only the fluid-dominated wave was captured in the experiment. In the model, the thickness of the PML was set to 0.0224 m and it was discretised with a spectral element of order 13. The solution time for one frequency step was 24.2 ms.

The results are presented in Fig. 6 and show very good agreement with the experimental data. Additionally, we plotted dispersion curves obtained from an analytical model developed for low frequency fluid-dominated waves with compact coupling with the soil [12]. The difference between the developed model and that from [12] becomes evident in the attenuation curve above 500 Hz. This can be attributed to several factors, the most important of which is that the analytical model does not consider loss related to shear effects in the pipe wall. It is also noted that it was difficult to extract the attenuation from the experiment above 500 Hz.

### 6.2. Water-filled plastic pipe submerged in water

The last case study is for the same fluid-filled MDPE pipe, this time - submerged in water. The details of the experimental setup and data processing can be found in [10]. Both the dimensions and the material properties are the same as for the buried case. The thickness of the PML was set to 0.1394 m and it was meshed with one spectral element of order 13. The solution time for a single frequency step including mode sorting was 9 ms. The comparison between the presented model and the experimental data is given in Fig. 7 showing very good agreement for the wavenumber. Unfortunately, the attenuation curves could not be well resolved from the experiment owing to the wavenumber extraction procedure being very sensitive to sensor positioning.



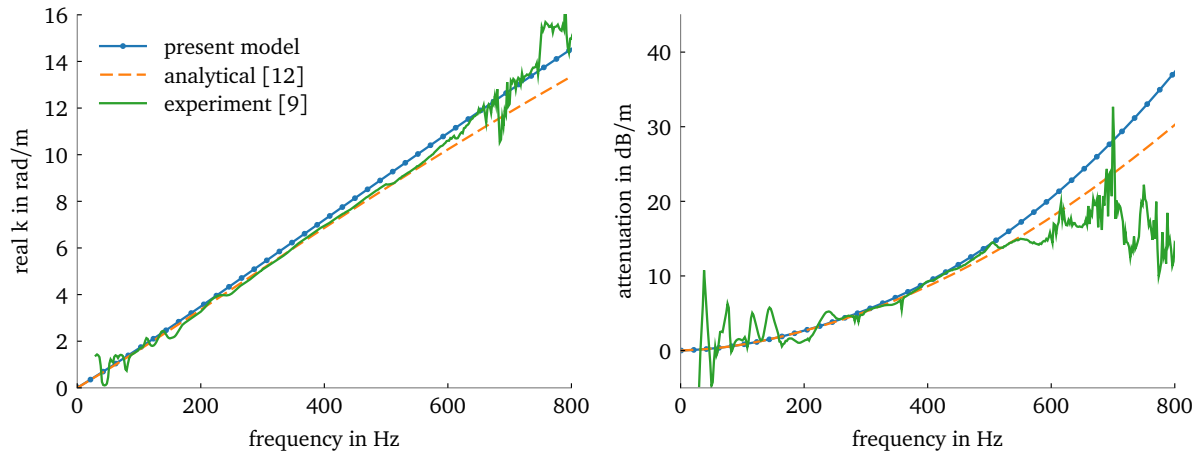


Figure 6: Wavenumber and attenuation for a water-filled MDPE pipe buried in soil (only the fluid-dominated wave); comparison between the present model, experiments [9] and an analytical model from [12].

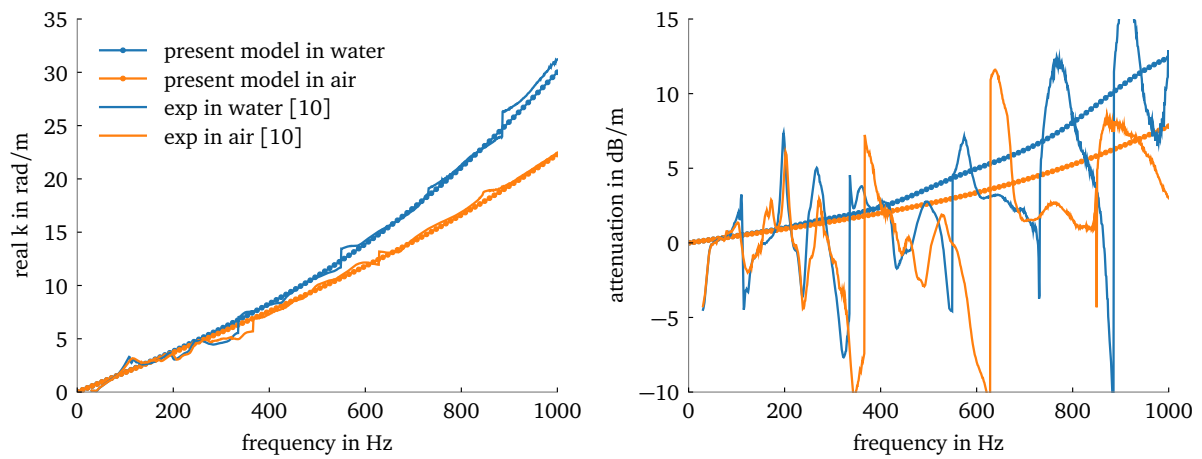


Figure 7: Wavenumber and attenuation for a water-filled MDPE pipe submerged in water (only the fluid-dominated wave); comparison between the present model and experiments[10].

## 7. Conclusions

A wave propagation model for axisymmetric fluid-filled embedded/submerged elastic waveguides was presented in this paper. It is based on the semi-analytical finite element principle, where only the cross-section is discretised using finite elements and spatial harmonicity of the displacement is assumed in the propagation direction. We derived an acoustic SAFE element and presented the coupling between the acoustic and structural elements. To enhance the efficiency of the solution, high-order spectral elements were used and singularities at the axis of symmetry were circumvented by using Gauss-Lobatto-Jacobi (0, 1) quadrature for core elements. The surrounding medium, either structural or acoustic, was modelled using a perfectly matched layer with an exponential stretching function. A procedure for determining PML parameters and the element order from the geometry and material properties of the system were derived and presented allowing for accurate predictions in both low and high frequency regimes, rather uncommon for PMLs. Finally, the validity of the model was demonstrated in three numerical verification cases against published results and two experimental case studies, all showing very good agreement. An implementation of the presented model in Python is made available with this article and relevant access details are given in the Acknowledgements section.

## Acknowledgements

The authors wish to thank Dr Nguyen Khac-Long (currently at INSA, Lyon) and Dr Hauke Gravenkamp (currently at University of Duisburg-Essen) for sharing the data from their publications.

Data access: The data supporting this study are openly available from the University of Southampton repository at <http://doi.org/10.5258/SOTON/D0282>.

Software access: An implementation of the presented model in Python is available at <https://doi.org/10.5281/zenodo.1025473>.

Funding: The support provided by the EPSRC (under grant EP/K021699/1) is gratefully acknowledged.

## Appendix A. Gauss-Lobatto-Jacobi (0, 1) quadrature

We first define  $x_{i,N}^{\alpha,\beta}$  as roots of a Jacobi polynomial  $P_N^{\alpha,\beta}(x)$ . These roots can be identified numerically, using a Newton-Raphson method. A very common algorithm is presented in Appendix B.2 of [41]. Of interest here is the (0, 1) quadrature, hence  $\alpha = 0$  and  $\beta = 1$ . The node locations are defined as

$$\xi_i = \begin{cases} -1 & \text{for } i = 1 \\ x_{i-1,N-2}^{1,2} & \text{for } 1 < i < N + 1 \\ 1 & \text{for } i = N \end{cases} \quad (\text{A.1})$$

whereas the associated weights as

$$w_i = \begin{cases} 2C_{1,N-2}^{0,1} & \text{for } i = 1 \\ C_{i,N-2}^{0,1} & \text{for } 1 < i < N \\ C_{N-1,N-2}^{0,1} & \text{for } i = N \end{cases} \quad (\text{A.2})$$

where

$$C_{i,N-2}^{0,1} = \frac{2^2 \Gamma(N) \Gamma(N+1)}{(N-1)(N-1)! \Gamma(N+2) [P_{N-1}^{0,1}(\xi_i)]^2} \quad (\text{A.3})$$

with  $\Gamma(x)$  being the generalised factorial.

The Langrangian interpolants through the nodes given above are defined as

$$h_i(\xi) = \begin{cases} \frac{2(-1)^{N-1}(\xi-1)[P_{N-1}^{0,1}(\xi)]'}{(N-1)N(N+1)} & \text{for } i = 1 \\ \frac{(\xi^2-1)[P_{N-1}^{0,1}(\xi)]'}{(N-1)(N+1)P_{N-1}^{0,1}(\xi_i)(\xi-\xi_i)} & \text{for } 1 < i < N \\ \frac{(1+\xi)[P_{N-1}^{0,1}(\xi)]'}{(N-1)(N+1)} & \text{for } i = N \end{cases} \quad (\text{A.4})$$

## Appendix B. Effective PML wavenumber

The full expression for the effective wavenumber at the termination of the PML is given in this section. Recalling that

$$e^{-jk_r \max \tilde{r}(r)} \Big|_{r=(d+h)} = e^{-j[\text{Re}(k_r \max) + j\text{Im}(k_r \max)] [d + \frac{h}{a}(e^a - 1) - j(\frac{h}{b}(e^b - 1)) + jh]} \quad (\text{B.1})$$

we can calculate the effective wavenumber by mapping the above expression onto

$$e^{-jk_{\text{PML}} r} \Big|_{r=(d+h)} \quad (\text{B.2})$$

Expanding the first equation and keeping the real parts only (as these are of primary interest here) we obtain

$$\text{Re}(k_r \max) \left[ d + \frac{h}{a}(e^a - 1) \right] + \text{Im}(k_r \max) \left[ \frac{h}{b}(e^b - 1) - h \right] = \text{Re}(k_{\text{PML}})(d+h) \quad (\text{B.3})$$

Further simplification yields

$$\text{Re}(k_{\text{PML}}) = \text{Re}(k_r \max) \left[ \underbrace{\frac{d}{d+h}}_{\text{term 1}} + \underbrace{\frac{h}{d+h} \frac{e^a - 1}{a}}_{\text{term 2}} + \underbrace{\frac{\text{Im}(k_r \max)}{\text{Re}(k_r \max)} \frac{h}{d+h} \left( \frac{e^b - 1}{b} - 1 \right)}_{\text{term 3}} \right] \quad (\text{B.4})$$

Let us now inspect the terms in square brackets in the light of the application to leaky wave problems. It is helpful to fix the parameters of the PML profile first. As it has been mentioned in Sec. 3.1,  $a = 6$  and  $b = 7$  give very good results for a variety of problems considered by the authors and it is expected that they suit well all typical leaky wave scenarios. Further to this, we can conclude that ‘term 3’ in Eq. (B.4) is not significant with respect to ‘term 2’ if  $|\text{Im}(k_{r \max})| < 0.2\text{Re}(k_{r \max})$ . This holds for lightly and moderately damped materials and when practical limiting guided wave attenuation is of interest. ‘Term 1’ may be comparable to ‘term 2’ for very thin PMLs ( $h < 0.1d$ ), but our presented method typically suggests choosing higher thicknesses.

For most practical cases, the following approximation yields satisfactory results

$$\text{Re}(k_{\text{PML}}) \approx \text{Re}(k_{r \max}) \frac{h}{d+h} \frac{e^a - 1}{a} \quad (\text{B.5})$$

The relationship between  $h$  and  $d$  may be verified after the calculation, and if  $h$  is returned very thin ( $< 0.1$ ) as compared to  $d$ , a more conservative expression can be used

$$\text{Re}(k_{\text{PML}}) \approx \text{Re}(k_{r \max}) \left( \frac{d}{d+h} + \frac{h}{d+h} \frac{e^a - 1}{a} \right) \quad (\text{B.6})$$

## References

- [1] M. J. S. Lowe, D. N. Alleyne, P. Cawley, Defect detection in pipes using guided waves, *Ultrasonics* 36 (1) (1998) 147–154. doi:10.1016/S0041-624X(97)00038-3.  
URL <http://www.sciencedirect.com/science/article/pii/S0041624X97000383>
- [2] J. L. Rose, A Baseline and Vision of Ultrasonic Guided Wave Inspection Potential, *Journal of Pressure Vessel Technology* 124 (3) (2002) 273–282.
- [3] C. R. Fuller, F. J. Fahy, Characteristics of wave propagation and energy distributions in cylindrical elastic shells filled with fluid, *Journal of Sound and Vibration* 81 (4) (1982) 501–518. doi:10.1016/0022-460X(82)90293-0.  
URL <http://www.sciencedirect.com/science/article/pii/0022460X82902930>
- [4] J. Greenspon, Axially Symmetric Vibrations of a Thick Cylindrical Shell in an Acoustic Medium, *The Journal of the Acoustical Society of America* 32 (8) (1960) 1017–1025. doi:10.1121/1.1908266.  
URL <http://asa.scitation.org/doi/10.1121/1.1908266>
- [5] B. Sinha, T. Plona, S. Kostek, S. Chang, Axisymmetric wave propagation in fluid-loaded cylindrical shells. I: Theory, *The Journal of the Acoustical Society of America* 92 (2) (1992) 1132–1143. doi:10.1121/1.404040.  
URL <http://asa.scitation.org/doi/abs/10.1121/1.404040>
- [6] K. Toki, S. Takada, Earthquake response analysis of underground tubular structure, *Bulletin of the Disaster Prevention Research Institute* 24 (2) (1974) 107–125.  
URL <http://repository.kulib.kyoto-u.ac.jp/dspace/handle/2433/124841>
- [7] A. N. Jette, J. G. Parker, Surface displacements accompanying the propagation of acoustic waves within an underground pipe, *Journal of Sound and Vibration* 69 (2) (1980) 265–274. doi:10.1016/0022-460X(80)90611-2.  
URL <http://www.sciencedirect.com/science/article/pii/0022460X80906112>
- [8] J. M. Muggleton, M. J. Brennan, R. J. Pinnington, Wavenumber prediction of waves in buried pipes for water leak detection, *Journal of Sound and Vibration* 249 (5) (2002) 939–954. doi:10.1006/jsvi.2001.3881.  
URL <http://www.sciencedirect.com/science/article/pii/S0022460X01938817>

- [9] J. M. Muggleton, M. J. Brennan, P. W. Linford, Axisymmetric wave propagation in fluid-filled pipes: wavenumber measurements in in vacuo and buried pipes, *Journal of Sound and Vibration* 270 (1–2) (2004) 171–190. doi: 10.1016/S0022-460X(03)00489-9.  
URL <http://www.sciencedirect.com/science/article/pii/S0022460X03004899>
- [10] J. M. Muggleton, M. J. Brennan, Leak noise propagation and attenuation in submerged plastic water pipes, *Journal of Sound and Vibration* 278 (3) (2004) 527–537. doi:10.1016/j.jsv.2003.10.052.  
URL <http://www.sciencedirect.com/science/article/pii/S0022460X03013270>
- [11] J. M. Muggleton, J. Yan, Wavenumber prediction and measurement of axisymmetric waves in buried fluid-filled pipes: Inclusion of shear coupling at a lubricated pipe/soil interface, *Journal of Sound and Vibration* 332 (5) (2013) 1216–1230. doi:10.1016/j.jsv.2012.10.024.  
URL <http://www.sciencedirect.com/science/article/pii/S0022460X12008255>
- [12] Y. Gao, F. Sui, J. M. Muggleton, J. Yang, Simplified dispersion relationships for fluid-dominated axisymmetric wave motion in buried fluid-filled pipes, *Journal of Sound and Vibration* 375 (2016) 386–402. doi:10.1016/j.jsv.2016.04.012.  
URL <http://www.sciencedirect.com/science/article/pii/S0022460X16300463>
- [13] J. M. Muggleton, M. Kalkowski, Y. Gao, E. Rustighi, A theoretical study of the fundamental torsional wave in buried pipes for pipeline condition assessment and monitoring, *Journal of Sound and Vibration* 374 (2016) 155–171. doi: 10.1016/j.jsv.2016.03.035.  
URL <http://www.sciencedirect.com/science/article/pii/S0022460X16300104>
- [14] M. Lowe, Matrix Techniques for Modeling Ultrasonic Waves in Multilayered Media, *IEEE Transactions on Ultrasonics, Ferroelectrics, and Frequency Control* 42 (4) (1995) 525–542. doi:10.1109/58.393096.
- [15] B. Pavlakovic, M. Lowe, D. Alleyne, P. Cawley, Disperse: A General Purpose Program for Creating Dispersion Curves, in: D. O. Thompson, D. E. Chimenti (Eds.), *Review of Progress in Quantitative Nondestructive Evaluation*, no. 16 in *Review of Progress in Quantitative Nondestructive Evaluation*, Springer US, 1997, pp. 185–192, doi: 10.1007/978-1-4615-5947-4\_24.  
URL [http://link.springer.com/chapter/10.1007/978-1-4615-5947-4\\_24](http://link.springer.com/chapter/10.1007/978-1-4615-5947-4_24)
- [16] B. Pavlakovic, *Leaky Guided Ultrasonic Waves in NDT*, PhD, Imperial College of Science, Technology and Medicine. University of London (1998).
- [17] I. Bartoli, A. Marzani, F. Lanza di Scalea, E. Viola, Modeling wave propagation in damped waveguides of arbitrary cross-section, *Journal of Sound and Vibration* 295 (3-5) (2006) 685–707. doi:10.1016/j.jsv.2006.01.021.  
URL <http://linkinghub.elsevier.com/retrieve/pii/S0022460X06001179>
- [18] A. Marzani, Time-transient response for ultrasonic guided waves propagating in damped cylinders, *International Journal of Solids and Structures* 45 (25–26) (2008) 6347–6368. doi:10.1016/j.ijsolstr.2008.07.028.  
URL <http://www.sciencedirect.com/science/article/pii/S0020768308003089>
- [19] M. Castaings, M. Lowe, Finite element model for waves guided along solid systems of arbitrary section coupled to infinite solid media, *The Journal of the Acoustical Society of America* 123 (2) (2008) 696–708. doi:10.1121/1.2821973.  
URL <http://scitation.aip.org/content/asa/journal/jasa/123/2/10.1121/1.2821973>
- [20] H. Jia, M. Jing, J. Rose, Guided wave propagation in single and double layer hollow cylinders embedded in infinite media, *The Journal of the Acoustical Society of America* 129 (2) (2011) 691–700. doi:10.1121/1.3531807.  
URL <http://scitation.aip.org/content/asa/journal/jasa/129/2/10.1121/1.3531807>
- [21] M. Mazzotti, I. Bartoli, A. Marzani, E. Viola, A coupled SAFE-2.5d BEM approach for the dispersion analysis of damped leaky guided waves in embedded waveguides of arbitrary cross-section, *Ultrasonics* 53 (7) (2013) 1227–1241. doi: 10.1016/j.ultras.2013.03.003.  
URL <http://www.sciencedirect.com/science/article/pii/S0041624X13000668>
- [22] M. Mazzotti, I. Bartoli, A. Marzani, Ultrasonic leaky guided waves in fluid-coupled generic waveguides: hybrid finite-boundary element dispersion analysis and experimental validation, *Journal of Applied Physics* 115 (14) (2014) 143512.

- doi:10.1063/1.4870857.  
 URL <http://scitation.aip.org/content/aip/journal/jap/115/14/10.1063/1.4870857>
- [23] M. Mazzotti, I. Bartoli, G. Castellazzi, A. Marzani, Computation of leaky guided waves dispersion spectrum using vibroacoustic analyses and the Matrix Pencil Method: A validation study for immersed rectangular waveguides, *Ultrasonics* 54 (7) (2014) 1895–1898. doi:10.1016/j.ultras.2014.05.009.  
 URL <http://www.sciencedirect.com/science/article/pii/S0041624X14001279>
- [24] J.-P. Berenger, A perfectly matched layer for the absorption of electromagnetic waves, *Journal of Computational Physics* 114 (2) (1994) 185–200. doi:10.1006/jcph.1994.1159.  
 URL <http://www.sciencedirect.com/science/article/pii/S0021999184711594>
- [25] F. Treysède, K. L. Nguyen, A. S. Bonnet-BenDhia, C. Hazard, Finite element computation of trapped and leaky elastic waves in open stratified waveguides, *Wave Motion* 51 (7) (2014) 1093–1107. doi:10.1016/j.wavemoti.2014.05.003.  
 URL <http://www.sciencedirect.com/science/article/pii/S0165212514000742>
- [26] K. L. Nguyen, F. Treysède, C. Hazard, Numerical modeling of three-dimensional open elastic waveguides combining semi-analytical finite element and perfectly matched layer methods, *Journal of Sound and Vibration* 344 (2015) 158–178. doi:10.1016/j.jsv.2014.12.032.  
 URL <http://www.sciencedirect.com/science/article/pii/S0022460X14010360>
- [27] F. Treysède, Spectral element computation of high-frequency leaky modes in three-dimensional solid waveguides, *Journal of Computational Physics* 314 (2016) 341–354. doi:10.1016/j.jcp.2016.03.029.  
 URL <http://www.sciencedirect.com/science/article/pii/S0021999116001819>
- [28] W. Duan, R. Kirby, P. Mudge, T.-H. Gan, A one dimensional numerical approach for computing the eigenmodes of elastic waves in buried pipelines, *Journal of Sound and Vibration* 384 (2016) 177–193. doi:10.1016/j.jsv.2016.08.013.  
 URL <http://www.sciencedirect.com/science/article/pii/S0022460X16304011>
- [29] P. Zuo, X. Yu, Z. Fan, Numerical modeling of embedded solid waveguides using SAFE-PML approach using a commercially available finite element package, *NDT & E International* 90 (2017) 11–23. doi:10.1016/j.ndteint.2017.04.003.  
 URL <http://www.sciencedirect.com/science/article/pii/S0963869517302414>
- [30] H. Gravenkamp, C. Birk, C. Song, The computation of dispersion relations for axisymmetric waveguides using the Scaled Boundary Finite Element Method, *Ultrasonics* 54 (5) (2014) 1373–1385. doi:10.1016/j.ultras.2014.02.004.  
 URL <https://www.sciencedirect.com/science/article/pii/S0041624X14000353>
- [31] H. Gravenkamp, C. Birk, C. Song, Computation of dispersion curves for embedded waveguides using a dashpot boundary condition, *The Journal of the Acoustical Society of America* 135 (3) (2014) 1127–1138. doi:10.1121/1.4864303.  
 URL <http://scitation.aip.org/content/asa/journal/jasa/135/3/10.1121/1.4864303>
- [32] H. Gravenkamp, C. Birk, C. Song, Numerical modeling of elastic waveguides coupled to infinite fluid media using exact boundary conditions, *Computers & Structures* 141 (2014) 36–45. doi:10.1016/j.compstruc.2014.05.010.  
 URL <http://www.sciencedirect.com/science/article/pii/S0045794914001242>
- [33] H. Gravenkamp, C. Birk, J. Van, Modeling ultrasonic waves in elastic waveguides of arbitrary cross-section embedded in infinite solid medium, *Computers & Structures* 149 (2015) 61–71. doi:10.1016/j.compstruc.2014.11.007.  
 URL <http://www.sciencedirect.com/science/article/pii/S0045794914002788>
- [34] P. Zuo, Z. Fan, SAFE-PML approach for modal study of waveguides with arbitrary cross sections immersed in inviscid fluid, *Journal of Sound and Vibration* 406 (2017) 181–196. doi:10.1016/j.jsv.2017.06.001.  
 URL <http://www.sciencedirect.com/science/article/pii/S0022460X17304637>
- [35] K.-J. Bathe, *Finite Element Procedures*, 2nd Edition, Klaus-Jurgen Bathe, Watertown, MA, 2006.
- [36] V. Damljanović, R. L. Weaver, Forced response of a cylindrical waveguide with simulation of the wavenumber extraction problem, *The Journal of the Acoustical Society of America* 115 (4) (2004) 1582. doi:10.1121/1.1675818.  
 URL <http://link.aip.org/link/JASMAN/v115/i4/p1582/s1&Agg=doi>
- [37] A. D. Pierce, *Acoustics: An Introduction to Its Physical Principles and Applications*, reprint Edition, Acoustical Society

- of America, 1989.
- [38] C. M. Nilsson, S. Finnveden, Waves in thin-walled fluid-filled ducts with arbitrary cross-sections, *Journal of Sound and Vibration* 310 (1-2) (2008) 58–76. doi:10.1016/j.jsv.2007.07.081.  
URL <http://www.sciencedirect.com/science/article/pii/S0022460X0700644X>
- [39] P. Kudela, M. Krawczuk, W. Ostachowicz, Wave propagation modelling in 1d structures using spectral finite elements, *Journal of Sound and Vibration* 300 (1-2) (2007) 88–100. doi:10.1016/j.jsv.2006.07.031.  
URL <http://www.sciencedirect.com/science/article/pii/S0022460X0600647X>
- [40] W. Ostachowicz, P. Kudela, M. Krawczuk, A. Żak, *Guided Waves in Structures for SHM: The Time-Domain Spectral Element Method*, John Wiley & Sons, Ltd, Chichester, 2012.
- [41] G. Karniadakis, S. J. Sherwin, *Spectral/hp Element Methods for CFD*, Oxford University Press, New York, Oxford, 1999.
- [42] M. I. Gerritsma, T. N. Phillips, Spectral Element Methods for Axisymmetric Stokes Problems, *Journal of Computational Physics* 164 (1) (2000) 81–103. doi:10.1006/j.cph.2000.6574.  
URL <http://www.sciencedirect.com/science/article/pii/S0021999100965744>
- [43] A. Fournier, *Incompressible Fluid Flows in Rapidly Rotating Cavities*, PhD thesis, 2004.
- [44] T. Nissen-Meyer, A. Fournier, F. A. Dahlen, A two-dimensional spectral-element method for computing spherical-earth seismograms - I. Moment-tensor source, *Geophysical Journal International* 168 (3) (2007) 1067–1092. doi:10.1111/j.1365-246X.2006.03121.x.  
URL <http://gji.oxfordjournals.org/content/168/3/1067>
- [45] A. Bottero, P. Cristini, D. Komatitsch, M. Asch, An axisymmetric time-domain spectral-element method for full-wave simulations: Application to ocean acoustics, *The Journal of the Acoustical Society of America* 140 (5) (2016) 3520–3530. doi:10.1121/1.4965964.  
URL <http://asa.scitation.org/doi/10.1121/1.4965964>
- [46] A. Bermúdez, L. Hervella-Nieto, A. Prieto, R. Rodríguez, An optimal perfectly matched layer with unbounded absorbing function for time-harmonic acoustic scattering problems, *Journal of Computational Physics* 223 (2) (2007) 469–488. doi:10.1016/j.jcp.2006.09.018.  
URL <http://www.sciencedirect.com/science/article/pii/S0021999106004487>
- [47] R. Cimpeanu, A. Martinsson, M. Heil, A parameter-free perfectly matched layer formulation for the finite-element-based solution of the Helmholtz equation, *Journal of Computational Physics* 296 (2015) 329–347. doi:10.1016/j.jcp.2015.05.006.  
URL <http://www.sciencedirect.com/science/article/pii/S0021999115003241>
- [48] F. Treysède, L. Laguerre, Numerical and analytical calculation of modal excitability for elastic wave generation in lossy waveguides, *The Journal of the Acoustical Society of America* 133 (6) (2013) 3827–3837. doi:10.1121/1.4802651.  
URL <http://scitation.aip.org/content/asa/journal/jasa/133/6/10.1121/1.4802651>
- [49] C. Aristégui, M. J. S. Lowe, P. Cawley, Guided waves in fluid-filled pipes surrounded by different fluids, *Ultrasonics* 39 (5) (2001) 367–375. doi:10.1016/S0041-624X(01)00064-6.  
URL <http://www.sciencedirect.com/science/article/pii/S0041624X01000646>
- [50] A. C. D. Royal, P. R. Atkins, M. J. Brennan, D. N. Chapman, H. Chen, A. G. Cohn, K. Y. Foo, K. F. Goddard, R. Hayes, T. Hao, P. L. Lewin, N. Metje, J. M. Muggleton, A. Naji, G. Orlando, S. R. Pennock, M. A. Redfern, A. J. Saul, S. G. Swingler, P. Wang, C. D. F. Rogers, Site Assessment of Multiple-Sensor Approaches for Buried Utility Detection, *International Journal of Geophysics* 2011 (2011) e496123. doi:10.1155/2011/496123.  
URL <https://www.hindawi.com/journals/ijge/2011/496123/abs/>
- [51] J. M. Muggleton, E. Rustighi, ‘Mapping the Underworld’: recent developments in vibro-acoustic techniques to locate buried infrastructure, *Géotechnique Letters* 3 (3) (2013) 137–141. doi:10.1680/geolett.13.00032.  
URL <http://www.icevirtuallibrary.com/doi/10.1680/geolett.13.00032>